Local and global bifurcations of a self-propelled heaving foil at high flapping frequencies

Luis Benetti Ramos[1] †, Olivier Marquet[1], Michel Bergmann [2,3] and Angelo Iollo[2,3]

[1]ONERA – The French Aerospace Lab, F-92190 Meudon, France

[2]Université de Bordeaux, IMB, UMR 5251, F-33400 Talence, France

[3]Equipe-projet Memphis, Inria Bordeaux-Sud Ouest, F-33400 Talence, France

(Received xx; revised xx; accepted xx)

When a foil is heaved along its symmetry axis and starts propelling in the orthogonal direction due to its interaction with the induced flow, complex self-propelled states may appear, as for instance a slow non-coherent back & forth motion of the foil at intermediate flapping frequency. We focus here on self-propelled states appearing for higher flapping frequencies, and, using time marching simulations, we report the existence of a new quasi-periodic self-propelled state when slightly increasing the frequency. Its propulsive wake does not only oscillate at the flapping frequency, but also slowly deviates upward and downward. When further increasing the frequency, the quasi-periodic oscillation disappears and a periodic and symmetric propulsive state is first obtained, followed by a permanently deviated propulsive state. To understand the emergence of these states, a time spectral method coupled to a pseudo arc-length continuation method is first used to follow the branch of periodic and symmetric propulsive solutions. It shows that, at high flapping frequency where the deviated propulsive solution is observed, this branch still exists, while a saddle-node bifurcation of periodic state occurs at lower frequency. The linear stability of these states is then investigated by performing a fluid-solid Floquet analysis. It reveals the existence of synchronous and asyncrhonous Floquet modes, both related to displacement of the wake vortices, that get unstable precisely when the periodic and quasi-periodic propulsive solutions are observed, respectively. If the transition from the symmetric propulsive solution to these two regimes is local in the sense of bifurcation analysis, the transition between the back & forth and quasi-periodic propulsive turns out to be global. By analyzing the evolution of this dynamic system through its phase space representation, we finally show that a collision between the two regimes occurs as it approaches the saddle-node bifurcation of the periodic symmetric branch.

Key words:

1. Introduction

The flapping wing propulsion adopted by aquatic and flying animals in nature Gray (1933); Wu (2010) offers nowadays a great source of inspiration for the conception of artificial swimmers Barrett (1996); Ramananarivo *et al.* (2013) and micro-aerial vehicles Ristroph & Childress (2014); Faux *et al.* (2018). A key problematic regarding the exploitation of this locomotion strategy concerns its emergence of non-coherent self-propelled regimes for certain imposed flapping movements. As observed in nature, living organisms such as sea butterflies that exploit flapping

† Email address for correspondence: luisbenettiramos@gmail.com

wing propulsion might sometimes present non-coherent motions during their flight Murphy *et al.* (2016), such as oscillatory motions around fixed points, which from an exploitation point of view are clear limitation due to the decrease of the locomotion efficiency and loss of trajectory control. To avoid this critical conditions, the self-propelled regimes of flapping wings and their transition is still an actively investigated problematic. To contribute to this study, the present work aims precisely at developing tools and a physical understanding of the transition between non-coherent and coherent self-propelled regimes of locomotion for a flapping wing.

In a previous work (Benetti Ramos *et al.* 2020) we have studied the emergence of flapping locomotion based on reciprocal motion. Our study revealed that the two self-propelled regimes that emerge from symmetric non-propulsive solutions, a periodic state of unidirectional motion and a quasi-periodic state of slow back & forth motion around a fixed position, can be explained by a fluid-solid Floquet stability analysis of the non-propulsive base-solution. A natural question that arises from this study is how this non-coherent back & forth solution can evolve for other control parameters. Authors in the past have followed different paths to investigate the suppression of non-coherent locomotion behaviours of self-propelled symmetrical foils in two-dimensional viscous fluids, revealing that a decrease of the thickness-to-chord aspect ratio h of ellipses and rectangular foils Zhang *et al.* (2009) or an increase of the solid-to-fluid density ratio of elliptical foils Lu & Liao (2006) can eventually turn non-coherent motions to unidirectional propulsion. However, regarding the exploitation of engineering devices, one of the most interesting paths followed in the literature might be the evolution of the self-propelled dynamics with a further increase of the flapping frequency Alben & Shelley (2005) or the flapping amplitude Deng & Caulfield (2015). In the case of elliptical foils with a fixed flapping amplitude immersed in a two-dimensional quiescent fluid, it has been shown that the increase of the flapping frequency can be explored to bring back the dynamics of the self-propelled foil to a coherent propulsion Alben & Shelley (2005). Using unsteady nonlinear simulations, we revisit in this work the nonlinear regimes of locomotion for a thin rectangular foil of nondimensional thickness-to-chord aspect ratio $h = 0.05$, solid-to-fluid density ratio $\rho = 100$ and flapping at a constant chord-based amplitude $A = 0.5$. By varying the Stokes number $\beta = f^*(c^*)^2/\nu$, a nondimensional number that uses the flapping frequency f^*, the foil chord c^* and the fluid kinematic viscosity ν as characteristic scales, in the range $10 \leqslant \beta \leqslant 40$ we carefully characterize and identify the transition between different self-propelled regimes of the foil motion: the back & forth motion around a fixed point (previously studied in (Benetti Ramos *et al.* 2020)) and three new regimes of unidirectional propulsion: a deviated quasi-periodic wake, a symmetric periodic wake and a deviated periodic wake propulsive regime. This parametric investigation accurately determines the Stokes number thresholds of these nonlinear regimes, that will then used for comparison with the second objective of this work: predicting the transition between these regimes using nonlinear and linear stability analyses.

Floquet stability analysis is a useful method to study the linear stability of periodic solutions and the onset of quasi-periodicity Floquet (1883). This analysis has been recently employed by Deng *et al.* (2016); Deng & Caulfield (2018) to study the transition between back & forth motions and unidirectional propulsive self-propelled regimes of a three-dimensional ellipsoid immersed in a quiescent fluid. Studying the stability of the initially axisymmetric base-flow surrounding a non-propelled flapping ellipsoid to azimuthally and time periodic perturbations Deng *et al.* (2016) found that the flow symmetry is initially broken by several high wave number modes and that increasing the flapping frequency, the leading unstable mode progressively becomes a purely left-right asymmetric mode. They associated the presence of these high azimuthal unstable modes to the non-coherent self-propelled regimes of locomotion of the flapping ellipsoid in Deng & Caulfield (2018). In our recent work (Benetti Ramos *et al.* 2020) we have addressed the emergence of the self-propelled regimes of locomotion by including into the Floquet stability analysis its

inherent fluid-solid coupling, instead of applying a purely-hydrodynamic analysis as previously done by Deng & Caulfield (2015); Deng *et al.* (2016); Deng & Caulfield (2018). In this work we will apply the same fluid-solid Floquet stability analysis to investigate the onset of deviated quasi-periodic wake, symmetric periodic wake and deviated periodic wake propulsive solutions for higher Stokes numbers. We will show, however, that different than our previous study this stability analysis can neither predict the onset of these three new unidirectional propulsive regimes or highlight linear mechanisms that lead to their emergence.

We will thus recur to nonlinear continuation methods to study the transition between these propulsive regimes, particularly following the symmetric periodic wake solutions that exist between the deviated quasi-periodic wake and deviated periodic wake propulsive regimes to understand these transition. The alternative here explored to compute unstable periodic solutions is to use their intrinsic periodicity to calculate directly the periodic limit cycle rather than undergoing temporal simulations. This fact is particularly useful when unstable limit cycles are sought, since in unsteady nonlinear simulations small perturbations introduced by the numerical method will be amplified during its temporal evolution and the solution will drift away from the unstable periodic cycle. In this work we will perform Time-Spectral Methods Gopinath & Jameson (2005); Sicot *et al.* (2008) coupled to pseudo arc-length methods Govaerts (2000) to follow the periodic solutions. Another possible strategies would be to apply time-delayed feedback methods, such as the one proposed by Shaabani-Ardali *et al.* (2017) and applied in Shaabani-Ardali *et al.* (2019) to filter sub-harmonic perturbations of a round jet, studying the emergence of vortex pairing as a global Floquet instability or by Jallas *et al.* (2017) to study the wake deviation of a non-propelled pitching foil.

This work is thus organized in four distinct parts. At first, unsteady nonlinear simulations are performed, §2.2, and the self-propelled regimes evolution for higher flapping frequencies is described. The transitions between regimes of non-propulsive, back & forth motion and deviated quasi-periodic wake, symmetric periodic wake and deviated periodic wake propulsion are identified for $10 \leqslant \beta \leqslant 40$. These results are followed by the stability analysis of symmetric non-propulsive solutions at this Stokes number range in §A. In §3 nonlinear bifurcation methods, time spectral method coupled to pseudo arc-length continuation, are used to follow symmetric periodic wake propulsive solutions. Their fluid-solid Floquet stability is thus analysed. This section is concluded by the analysis of the unstable regions and the obtained quasi-periodic and periodic wake deviation modes. We finally regard the transition between two quasi-periodic regimes, the back & forth and deviated quasi-periodic wake propulsive solutions in §4.

2. Problem formulation and self-propelled nonlinear solutions

We investigate in this work the horizontal self-propulsion of a heaving symmetric rectangular foil. The rigid body has a rectangular shape with rounded edges and is characterized by its chord $c = 1$ and its non-dimensional thickness $h = h^*/c$ (where * is adopted to differentiate dimensional and nondimensional parameters) with the round edges being of diameter equivalent to the foil thickness. The foil nondimensional foil surface is thus defined as $S = (1 - h)h + \pi h^2/4$ and it has an uniform density ρ_s. This body translates in an initially quiescent two-dimensional fluid of density ρ_f and kinematic viscosity ν with a velocity $\mathbf{u}_g = (u_g, v_g)$. This velocity is partially imposed through the vertical heaving motion $y_g^*(t) = -A^* \cos(2\pi f^* t^*)$, and partially free along the horizontal axis as a result of hydrodynamic forces acting on the solid-fluid interface Γ_w.

This rigid-body fluid-structure interaction is characterized by four non-dimensional parameters: the frequency-based Stokes number β, the non-dimensional amplitude A, the solid-fluid density ratio ρ and the non-dimensional thickness h, defined respectively as

$$\beta = \frac{f^* c^2}{\nu},\ A = \frac{A^*}{c},\ \rho = \frac{\rho_s}{\rho_f} \text{ and } h = \frac{h^*}{c}\,. \tag{2.1}$$

The non-dimensional flapping period T is thus equal to 1 whatever the values of the Stokes number β due to the choice of characteristic time-length. The surrounding fluid, absolute fluid velocity $\mathbf{u} = (u, v)$ and pressure p, is governed by the two-dimensional incompressible Navier-Stokes equations

$$\frac{\partial \mathbf{u}}{\partial t} = -\boldsymbol{\nabla}\mathbf{u}\cdot(\mathbf{u}-\mathbf{u}_g) - \boldsymbol{\nabla} p + \beta^{-1}\boldsymbol{\Delta}\mathbf{u}\,,\ \boldsymbol{\nabla}\cdot\mathbf{u} = 0\,, \tag{2.2}$$

written in the non-inertial frame of reference that follows the foil center of mass G as done in other fluid-structure interactions studies, such as falling and rising bodies in fluids (Jenny *et al.* 2003; Tchoufag *et al.* 2014) or pitching foils (Jallas *et al.* 2017). The body is self-propelled and the evolution of its horizontal motion is governed by Newton's second law

$$\frac{\mathrm{d}u_g}{\mathrm{d}t} = (\rho S)^{-1} F_x(\mathbf{u}, p)\ ,\ F_x(\mathbf{u}, p) = \int_{\Gamma_w} ([-p\mathbf{I} + \beta^{-1}(\boldsymbol{\nabla}\mathbf{u} + \boldsymbol{\nabla}^T\mathbf{u})]\cdot\mathbf{n})\cdot\mathbf{e}_x \mathrm{d}\Gamma_w\,, \tag{2.3}$$

where $\mathbf{n}$ is the outward normal. Equations (2.2) and (2.3) are closed by a no-slip boundary condition on the foil surface $\mathbf{u}(\Gamma_w, t) = \mathbf{u}_g(t)$. This equations can be cast in a compact for using the system state variable $\mathbf{q} = [\mathbf{u}, p, u_g]^T$

$$\mathcal{B}\frac{\partial \mathbf{q}}{\partial t} = \mathcal{R}(\mathbf{q}, v_g)\,, \tag{2.4}$$

where the operators $\mathcal{B}$ and $\mathcal{R}$ are respectively the system mass-matrix (that select the appropriate time-derivatives) and the spatial operator that contains the Navier-Stokes equations and the Newton's second law.

2.1. *Numerical method*

The system of equations (2.4) is discretized in time using the following r-order semi-implicit scheme

$$\begin{aligned}
\frac{\alpha_0}{\Delta t}\mathbf{u}^{n+1} + \nabla p^{n+1} - \beta^{-1}\Delta\mathbf{u}^{n+1} &= \mathbf{f}^{n+1} \\
\nabla\cdot\mathbf{u}^{n+1} &= 0 \\
(u^{n+1}, v^{n+1})(\Gamma_w) &= \left(u_g^{n+1}, 2\pi\, A\, sin(2\pi t^{n+1})\right) \\
(\rho S)\frac{\alpha_0}{\Delta t}u_g^{n+1} &= F_x(\mathbf{u}^{n+1}, p^{n+1}) - \sum_{k=1}^{r}\frac{\alpha_k}{\Delta t}u_g^{n+1-k} \\
(u^{n+1}, v^{n+1})(\Gamma_e) &= (0, 0),
\end{aligned} \tag{2.5}$$

where the linear diffusion terms are implicit and the nonlinear convective terms are explicit, with the right-hand side forcing term $\mathbf{f}^{n+1}$ in the momentum equation defined as

$$\mathbf{f}^{n+1} = -\sum_{k=1}^{r}\gamma_k(\mathbf{u}^{n+1-k} - \mathbf{u_g}^{n+1-k})\cdot\nabla\mathbf{u}^{n+1-k} - \sum_{k=1}^{r}\frac{\alpha_k}{\Delta t}\mathbf{u}^{n+1-k}\,,$$

with Δt the time step and $(\mathbf{u}^{n+1}, p^{n+1})$ the velocity and pressure at time $t_{n+1} = (n+1)\Delta t$. The time derivatives (nonlinear convection terms) are approximated (extrapolated) by r-order backward differential formulae. A first-order scheme ($r = 1$, $\alpha_0 = 1$, $\alpha_1 = -1$ and $\gamma_1 = 1$) is used for the first two temporal iterations ($n \leqslant 1$), followed by a second-order scheme ($r = 2$, $\alpha_0 = 3/2$,

$\alpha_1 = -2$, $\alpha_2 = 1/2$, $\gamma_1 = 2$ and $\gamma_2 = -1$). The equality of fluid and solid velocity is treated implicitly, to avoid time-step restrictions induced by an explicit coupling (Causin *et al.* 2005). To allow the use of an existing fast implementation of the flow equations Jallas *et al.* (2017), we use the segregated approach proposed by Jenny & Dušek (2004). Typically, the time step is set to $\Delta t = 5 \cdot 10^{-4}$ for small values of the Stokes number ($\beta = 19$) and is decreased to $\Delta t = 2.5 \cdot 10^{-4}$ for larger values ($\beta = 32$), so as to ensure the numerical stability of this semi-explicit temporal scheme (Kress & Lötstedt 2006).

A continuous Galerkin finite-element method is thus employed to discretize the equations (2.5) in space. Quadratic elements (P2) and linear elements (P1) are respectively used for the flow velocity and the pressure. The implementation is based on the FreeFEM software (Hecht 2012). A circle of (non-dimensional) diameter 60 centered at the foil center of mass is used as computational domain, with its external boundary denoted Γ_e. A Delaunay triangulation of the computational domain results in a mesh with typically 3.3×10^4 triangles. To create a mesh that is symmetric with respect to the y-axis and refined in flow regions exhibiting large velocity gradients we have proceed as follows. Once a first solution has been computed, we adapt a mesh of a half domain to several instants of the periodic flow, using the hessian-based mesh adaptation implemented in FreeFEM (see Fabre *et al.* (2018) for a practical review). This mesh is thus duplicated to assemble the full mesh. The triangle size is typically of order $O(10^{-2})$ close to the foil and over the wake behind the foil, and 1 in the external part of the domain. Mesh refinement and domain size were chosen based on the convergence of the foil horizontal velocity and the vertical hydrodynamic force. Greater domains or mesh refinement have exhibited little influence over these values. The validation of this numerical method is detailed in (Benetti Ramos *et al.* 2020).

2.2. *Three propulsive self-propelled solutions at higher Stokes numbers*

Unsteady nonlinear simulations are performed for values of the Stokes numbers in the range $15 \leqslant \beta \leqslant 35$. The other control parameters - flapping amplitude $A = 0.5$, the density ratio $\rho = 100$ and the foil aspect ratio $h = 0.05$ - are kept fixed. When increasing the Stokes number four distinct self-propelled solutions are obtained: back & forth solutions – that will not be discussed here in this work since they have been exposed in a previous work (Benetti Ramos *et al.* 2020) and are briefly described in §4 – (1) deviated quasi-periodic wake (DQPW), (2) reversed Von-Kárman wake (SPW) and (3) deviated periodic wake (DPW) propulsive solutions. These three additional regimes propulsive regimes are characterized hereafter. In figure 1 we characterize the unsteady flow of these propulsive regimes through the out-of-plane vorticity ω_z for three representative values of Stokes number, respectively $\beta = 21$ for the DQPW, $\beta = 23$ for the SPW and $\beta = 30$ for the DPW propulsive solution. Although all solutions here after presented have positive velocities, negative velocities are equally attainable depending on the initial condition, with the choice for positive velocities being a mere convention determinated by a positive initial velocity perturbation imposed to the system.

Owing to their unidirectional propulsive character these solutions present all a non spatially symmetric flow. In all three regimes we observe the formation of a vortex wake behind the foil trailing edge, with this vortex wake having very different dynamics in each case. For DQPW solutions (1-i) only a small wake consisting of a vortex dipole is seen. The distance separating successive vortex is very small, and the dipole is periodically deviated upward (downward) as it can be seen in the first (second) row of the figure. The quasi-periodic nature of this regime is precisely linked to the cyclic alternation between upward and downward wake deviation. When the Stokes number is increased, the distance separating successive vortex is increased and the

(i) Deviated quasi-periodic wake (DQPW) propulsive solution

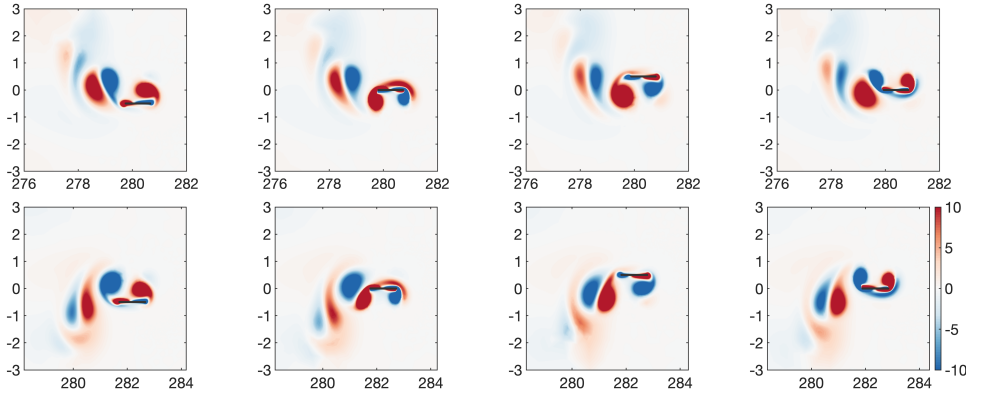

(ii) Symmetric periodic wake (SPW) propulsive solution

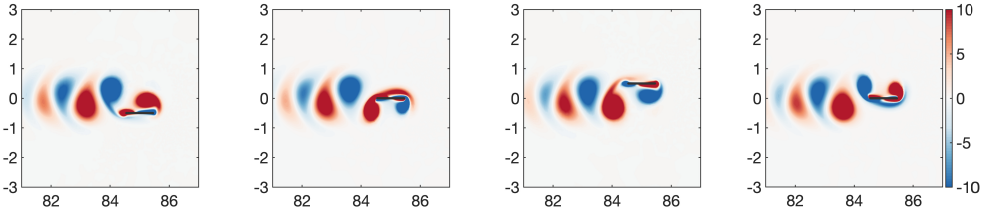

(iii) Deviated periodic wake (DPW) propulsive solution

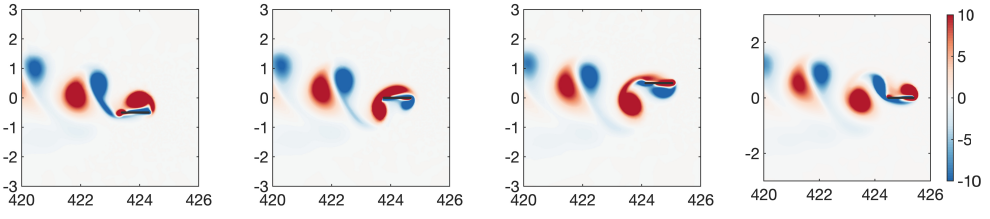

Figure 1: Vorticity snapshots for four equally spaced instants along a flapping period with the inital time being taken when $y_g = -0.5$ (shown at the next figure) for a (i) DQPW (first and second row starting at different initial instants), (ii) SPW and (iii) DPW propulsive solutions.

wake is neither constituted solely of a vortex dipole or presents a quasi-periodic wake deviation. The propulsive solution retrieves the spatio-temporal symmetry (Elston *et al.* 2004)

$$(u, v, p, \omega_z)(x, y, t) = (u, -v, p, -\omega_z)(x, -y, t + T/2)\,, \tag{2.6}$$

which is the combination of the y-reflection symmetry and the $T/2$ time-reciprocal translation, and symmetric periodic wake solutions (SPW) (1-ii) are thus obtained. These solutions feature a reversed Von-Kármán vortex street Triantafyllou *et al.* (1991), a clear sign of a propulsive solution since fluid is accelerated away from the foil. As the Stokes numbers is further risen, this vortex street start to form dipoles and the wake is no longer spatio-temporally symmetric with respect to the x-axis. Deviated periodic wake (DPW) propulsive solutions are thus obtained, figure 1

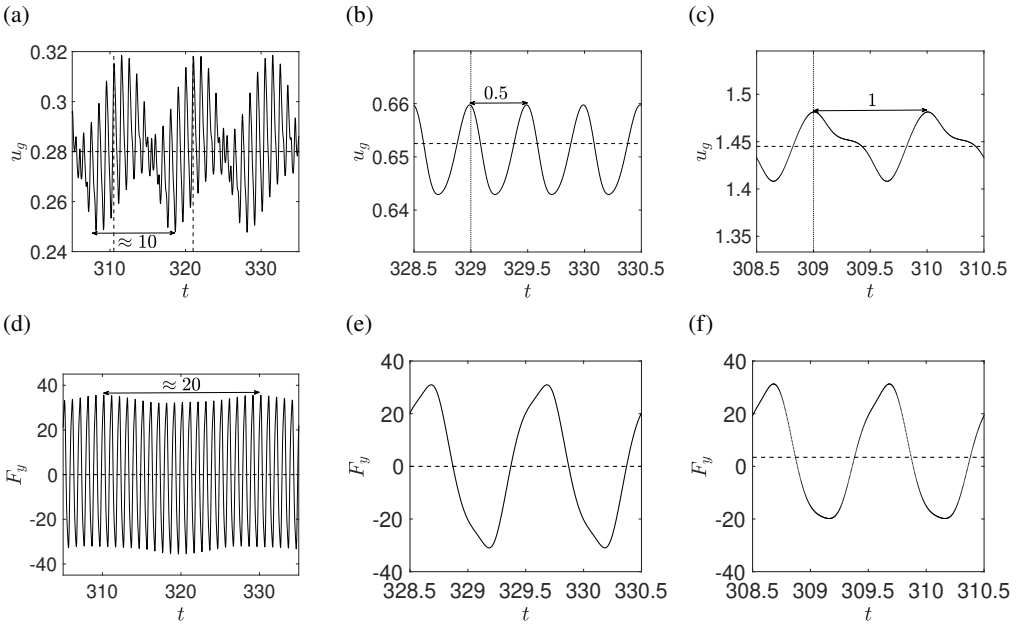

Figure 2: Temporal evolution of the (a-c) horizontal velocity u_g and (d-f) vertical force F_y of the foil for the (a,d) QP ($\beta = 21$), (b,e) SPW ($\beta = 23$) and (c,f) DPW ($\beta = 30$) propulsive solution. The temporal evolution is displayed during a flapping period but in (a,d) for a slow period. Horizontal dashed lines indicate the time-averaged value of the plotted quantity. Vertical lines indicate the initial times of figure 1in (a-c).

(iii), where we observe that vortex dipoles deviated in a positive y direction are shed away while the flapping wing advances in the positive x direction, and we remark that although the foil is self-propelled in our case, the deviation process is very similar to that observed for non-propelled flapping foils Godoy-Diana *et al.* (2009); Jallas *et al.* (2017).

Consistent to their contransting flow dynamics, these solutions present different self-propelled dynamics, that are characterized in figure 2 by the temporal evolution of their horizontal velocity and vertical force. The horizontal velocity of the DQPW solutions (2-a) oscillate around a non-zero time-averaged value mean value with two distinct periods – one identical to the imposed heaving movement, since the solution does not respect the spatio-temporal symmetry, and one of order $O(10^{-1})$, that is half the one of the vertical force (2-d). This difference is associated to the spatio-temporal symmetry of the cyclic upward and downward wake deviation – while the wake deviation shifts the time-averaged value of the vertical force along the (fast) flapping period between positive and negative values resp. for upward and downward deviations, the horizontal velocity is increased similarly in the two cases. The half period of the horizontal velocity can thus be understood in a similar way as the half flapping period presented by propulsive solutions that verify the spatio-temporal symmetry along the flapping period.

This is the case, for instance, in the horizontal velocity time signal of the SPW solution (2-b). The periodic propulsive solutions present a small amplitude oscillation around a non-zero time-averaged value with a period that is half the flapping one, due to the spatio-temporal symmetry of upward and downward flapping strokes. We observe that in this case, the time-averaged value reached by the horizontal velocity is much greater than the propulsive solutions existing for $4 \leqslant \beta \leqslant 9.58$ that were obtained in our previous study (Benetti Ramos *et al.* 2020), with the Reynolds number based on the time-averaged horizontal velocity $Re =< u_g > \beta$ reaching an

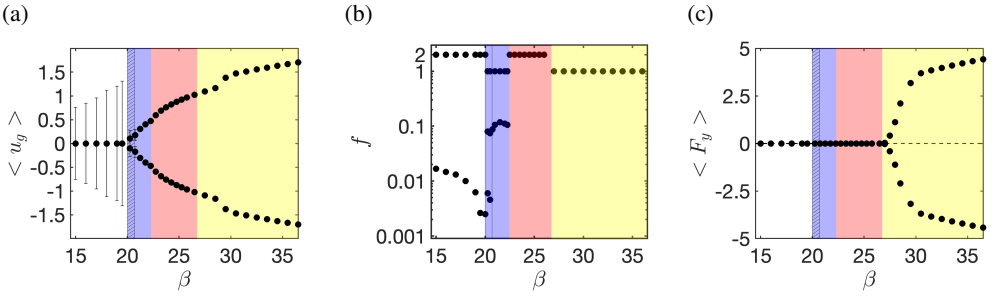

Figure 3: Evolution with β for $A = 0.5$ and $\rho = 100$ of the foil (a) mean horizontal speed (filled circles) and its amplitude (error bars) as well as (b) dominant frequency of this time signal, and (c) time-averaged vertical force. Violet, red and yellow areas are highlighted for the occurrence of respectively deviated quasi-periodic wake (DQPW), symmetric periodic wake (SPW) and deviated periodic wake (DPW) propulsive solutions. The hatched area indicates the transition between back & forth motion and DQPW solutions where two small frequencies remain (three frequencies in total).

order $10 - 100$, an increase of one order of magnitude when compared to the previous low Stokes number propulsive regime. Since this solution does not feature any wake deviation and respect thus the spatio-temporal symmetry, the vertical force acting on the foil goes through positive and negative values within a flapping period (2-e) around a zero time average due to symmetry of upward and downward half-strokes.

Once the spatio-temporal symmetry is lost due to the wake deviation, the DPW solution will present a frequency equal to the flapping one in both its horizontal velocity and vertical force, figure 2 (c) and (f). The remarkable distinction of the deviated wake periodic solution is the fact that upward (downward) wake deviation generates a non-zero positive (negative) time-averaged vertical force acting on the foil. This wake deviation, as the propulsion direction, can occur both in upward and downward directions depending solely on the initial conditions applied to the system.

(1) Deviated quasi-periodic wake (DQPW), (2) reversed Von-Kárman wake (SPW) and (3) deviated periodic wake (DPW) propulsive solutions are summarized in figure 3 respectively identified by violet, red and yellow background colors. The horizontal velocity is shown in (a) by its time-average value $< u_g >$ (represented by dots) and its amplitude (error bars). This time-average is executed along many periods, that in the case of quasi-periodic solutions enclose an entire slow period. The frequencies f of the horizontal velocity time signal are shown in (b) whereas the time-averaged vertical force $< F_y >$ is shown in (c). This summary is a detailed description of the return to coherent propulsion for a rectangular symmetric foil. A similar scenario that draw the frontier between non-propulsive and coherent or non-coherent propulsion has been made by Alben & Shelley (2005) for an ellipse of aspect ratio $h = 0.1$, flapping at a constant amplitude $A = 0.5$ for several density ratios in the range $1 \leqslant \rho \leqslant 100$. We remark, however, that the DQPW have not been described in this scenario being the great novelty of the present results.

As we can see from Figure 3, a coherent state of locomotion is retrieved for $\beta = 20$. This unidirectional propulsive solutions are retrieved after non-coherent back & forth motion around a fixed point, as is the case in Alben & Shelley (2005). Back & forth solutions, studied in detail in a previous work (Benetti Ramos *et al.* 2020) present a large amplitude of oscillation but zero time-averaged velocity featuring very small frequencies that tend to zero as β tends to 20. For $20 \leqslant \beta < 22.5$ deviated quasi-periodic wake propulsive solutions are obtained, with the quasi-periodic nature of the solution being retained. The quasi-periodicity nevertheless is associated to a periodic deviation of the wake behind the foil and not to the direction switching

as is the case of back & forth solutions. The characteristic frequencies of the DQPW solution is then a frequency of order 1, since the solution does not respect the spatio-temporal symmetry due to the wake deviation, and a frequency of $O(10^{-1})$ associated to the cyclic wake deviation. During a transition range ($20 \leqslant \beta \leqslant 20.5$), identified by a hatched path, the small frequency of order $O(10^{-2})$ of back & forth solutions is retained, and the self-propelled solutions possess three different characteristic frequencies over this range – this transitional regime will be further discussed in §4. For $22.5 \leqslant \beta < 27$ the quasi-periodic wake deviation behind the foil disappears, and propulsive solutions with a symmetric periodic wake (SPW) are obtained. SPW solutions are characterized by a non-zero time-averaged velocity and a frequency of twice the flapping one. Finally, this frequency becomes one when the wake spatio-temporal symmetry is broken for $\beta \geqslant 27$ where propulsive solutions with deviated periodic wakes (DPW) are obtained. This transition to wake deviation is captured due to the non-zero time-averaged vertical force of these solutions that is visible in figure 3(c). At the onset of DPW solutions we do not observe a particular increase of the time-averaged horizontal velocity. Nevertheless, a significant increase is obtained for $\beta \geqslant 29$. This velocity increase is not associated to any major transition in the self-propelled dynamics, with the only visible feature of the flow around the solutions being the fact that the wake deviation takes place immediately behind the foil trailing edge.

3. Local bifurcation of symmetric periodic wake propulsive solutions

The emergence of deviated quasi-periodic wake (DQPW) and deviated periodic wake (DPW) propulsive solutions is now investigated by analysing the continuation and the stability of symmetric periodic wake (SPW) propulsive solutions. The nonlinear bifurcation method that couples time-spectral method (TSM) to pseudo arc-length continuation is introduced in §3.1 followed by Floquet stability analysis §3.2. The results of SPW continuation and their stability are then presented (§3.3) by carefully describing the branch obtained through numerical continuation and its stability. This analysis is thus followed by the study of the unstable modes that are discussed in light of the previously described nonlinear self-propelled solutions.

3.1. *Time Spectral Method and Pseudo Arc-Length continuation*

The studied problem presents an inherent periodicity thanks to the imposed flapping movement which is retained by some of the nonlinear regimes seen in the previous section, i.e. the SPW propulsive solutions. Harmonic balance methods, such as the Time Spectral Method (TSM) Gopinath & Jameson (2005), can take advantage of this time-periodicity to solve directly for the periodic limit cycle rather than following the temporal evolution in unsteady nonlinear simulations up to saturation. This strategy consists on rewriting in a spectral form the originally unsteady problem eq. (2.4). An identical expression can be written for several time instants along a period

$$\mathbf{B}\frac{\partial Q}{\partial t} = \mathbf{R}(Q, v_g)\,, \tag{3.1}$$

where $\mathbf{B}$ is a matrix of diagonal entries equal to $\mathcal{B}$ and Q regroups $2N+1$ time instants

$$Q = \left[\mathbf{q}(\mathbf{x}, t_0), \mathbf{q}\left(\mathbf{x}, t_0 + \frac{1}{2N+1}\right), ..., \mathbf{q}\left(\mathbf{x}, t_0 + \frac{2N}{2N+1}\right)\right]^T\,, \tag{3.2}$$

and the vector $\mathbf{R}$ the related spatial operators

$$\mathbf{R} = \left[\mathcal{R}(\mathbf{q}(\mathbf{x}, t_0)), ..., \mathcal{R}\left(\mathbf{q}\left(\mathbf{x}, t_0 + \frac{2N}{2N+1}\right)\right)\right]^T\,. \tag{3.3}$$

These $2N+1$ instants are used to determine, following the Nyquist-Shannon criterion (Gopinath

& Jameson 2005), at best the spectral content of the periodic solution up to N harmonics, contained in the vector $\hat{Q}$

$$\hat{Q} = [\hat{\mathbf{q}}_{-N}(\mathbf{x}), ..., \hat{\mathbf{q}}_0(\mathbf{x}), ..., \hat{\mathbf{q}}_N(\mathbf{x})]^T , \tag{3.4}$$

through a discrete Fourier transform $\hat{Q} = \mathcal{F}Q$, and inversely the time instants can equally be determined through an inverse discrete Fourier transform $Q = \mathcal{F}^{-1}\hat{Q}$ with the discrete direct and inverse Fourier transforms defined as

$$\mathcal{F}_{n,k} = \frac{1}{2N+1} \exp\left(\frac{-i2k\pi(n-N)}{2N+1}\right), \; \mathcal{F}^{-1}_{n,k} = \exp\left(\frac{i2k\pi(n-N)}{2N+1}\right). \tag{3.5}$$

The continuous time-differential operator can thus be approximated by a discrete spectral time-domain equivalent as

$$\frac{\partial Q}{\partial t} \approx \frac{\partial}{\partial t}(\mathcal{F}^{-1}\hat{Q}) = \frac{\partial \mathcal{F}^{-1}}{\partial t}\hat{Q} = \underbrace{\mathcal{F}^{-1}\Lambda\mathcal{F}}_{\mathcal{D}_\omega} Q , \tag{3.6}$$

where $\Lambda_{n,n} = (i2\pi(n-N)/2N+1)$ is a diagonal matrix that contains the time-derivative of the inverse Fourier transform coefficients for the n-th harmonic and $\mathcal{D}_\omega$ is the spectral version (in time) of the time-differential operator composed of off-diagonal coefficients

$$(\mathcal{D}_\omega)_{i,j} = \begin{cases} \pi(-1)^{(i-j)} \csc\left(\dfrac{\pi(i-j)}{2N+1}\right), & \text{if } (i-j) \neq 0 \\ 0, & \text{if } (i-j) = 0 \end{cases} . \tag{3.7}$$

The system rewritten in a spectral form, cast in the time domain in the case of the TSM, couples all the time instants along a period

$$\mathcal{N}_{TSM}(Q) = \mathbf{B}\mathcal{D}_\omega Q - \mathbf{R}(Q, v_g) = 0 , \tag{3.8}$$

that couple all the time instants together. The Time Spectral Method transforms thus the unsteady system, eq. (2.4), into a stationary system (eq. (3.8)). The root of this stationary system can thus be sought through a proper method for solving nonlinear systems, such as the Newton's method. The great advantage of searching periodic limit cycles through a Newton method is that this method can obtain unstable roots of the system of equations. This is the case for example when the steady Navier-Stokes equation is solved for determining unstable base-flows (i.e. Sipp & Lebedev (2007); Tchoufag *et al.* (2014) and many others). The drawback from this method is that it results on a large scale linear system. To efficiently solve this problem we employ an iterative resolution of the resulting linear system that uses a preconditionning strategy based on the decomposition of the TSM Jacobian where we split the linearized spatial operator $\dfrac{\partial \mathcal{R}}{\partial Q}$ in a part that depends on the time-averaged over a flapping period $\langle Q \rangle$ and its fluctuation $\tilde{Q}$ to identify a block-circulant matrix $\mathbf{C} = \mathcal{D}_\omega - \dfrac{\partial \mathcal{R}}{\partial Q}(\langle Q \rangle)$. This circulant matrix, which is easily diagonalizable (Schmid *et al.* 2017) is then used as a preconditionner for the full TSM Jacobian matrix. The continuation of the solution through the variation of the Stokes number in our study was based on a pseudo arc-lenght continuation (Govaerts 2000), rather than a constant evolution of the Stokes number to avoid problems with possible turning points/ fold bifurcations.

The TSM has been cross-validated against the unsteady nonlinear solver employed in this work. Twenty-two harmonics have been necessary to reduce the L_1-norm of the difference of the

periodic-cycle obtained by the two-methods under 10^{-6} for a Stokes number of $\beta = 32$ and this value was thus employed throughout our entire study.

3.2. *Fluid-solid Floquet stability analysis of self-propelled foils*

Infinitesimal perturbations ($\epsilon \ll 1$) are superimposed to the periodic base solution $(\mathbf{u_b}, p_b, u_{g,b})$

$$(\mathbf{u}, p, u_g) = (\mathbf{u}_b, p_b, u_{g,b}) + \epsilon(\mathbf{u}', p', u_g'), \tag{3.9}$$

where both base-flow $(\mathbf{u}', p')$ and the foil horizontal velocity u_g' are perturbed. No perturbation of the vertical velocity $\mathbf{v}_g$ is considered since this movement is imposed. The dynamics of the perturbations are governed at leading order by the following system of equations

$$\mathcal{B}\,\frac{\partial}{\partial t}\underbrace{\begin{bmatrix}\mathbf{u}'\\ p'\\ u_g'\end{bmatrix}}_{\mathbf{q}'} = \underbrace{\begin{bmatrix} -\left[(\mathbf{u}_b(t)-\mathbf{u}_{g,b}(t))\cdot\boldsymbol{\nabla}\right] - \boldsymbol{\nabla}\mathbf{u}_b(t) + \beta^{-1}\boldsymbol{\Delta} & -\boldsymbol{\nabla} & (\boldsymbol{\nabla}\mathbf{u}_b)\cdot\mathbf{e}_x \\ -\boldsymbol{\nabla} & 0 & 0 \\ (\rho S)^{-1}\mathcal{F}_v & (\rho S)^{-1}\mathcal{F}_p & 0 \end{bmatrix}}_{\mathcal{L}(\mathbf{u}_b, p_b, \mathbf{u}_{g,b})} \begin{bmatrix}\mathbf{u}'\\ p'\\ u_g'\end{bmatrix} \tag{3.10}$$

The first two rows are the linearized momentum and mass equations governing the fluid velocity and pressure perturbations. They are coupled to the foil velocity perturbation u_g' via two terms: firstly, the bulk term $(\boldsymbol{\nabla}\mathbf{u}_b)\cdot\mathbf{e}_x$ (block $(1,3)$ in the right-hand side matrix) that modifies the production of fluid perturbation in the momentum equation, and secondly, the boundary conditions at the foil surface Γ_w, where the equality of fluid and solid perturbations holds

$$(u', v')(\mathbf{x}_w, t) = (u_g', 0)\,. \tag{3.11}$$

The third row indicates that the horizontal acceleration of the foil is equal to the horizontal force exerted by the flow perturbation, which is here separated into viscous $\mathcal{F}_v$ and pressure $\mathcal{F}_p$ contributions, respectively defined as

$$\mathcal{F}_v(\mathbf{u}') = \beta^{-1}\int_{\Gamma_w}(\nabla\mathbf{u}' + \nabla\mathbf{u}'^T)\cdot\mathbf{n})\cdot\mathbf{e}_\mathbf{x}\,\mathrm{d}\Gamma_w \quad , \quad \mathcal{F}_p(p') = \int_{\Gamma_w}(-p'\mathbf{n})\cdot\mathbf{e}_\mathbf{x}\,\mathrm{d}\Gamma_w\,. \tag{3.12}$$

Following Elston *et al.* (2004) or Jallas *et al.* (2017), the perturbations are further decomposed in the form

$$\mathbf{q}'(\mathbf{x}, t) = \sum\left(\hat{\mathbf{q}}_j(\mathbf{x}, t)e^{\lambda_j t} + \text{c.c.}\right), \tag{3.13}$$

where $\hat{\mathbf{q}}_j$ are T-periodic functions, called the Floquet modes, associated to the complex numbers λ_j, called the Floquet exponents. The Floquet multiplier $\mu_j = e^{\lambda_j T}$, rather used in the following, represents the complex amplitude gain of the periodic Floquet mode over one period, i.e. $\hat{\mathbf{q}}_j(\mathbf{x}, T) = \mu_j\hat{\mathbf{q}}_j(\mathbf{x}, 0)$. The Floquet multiplier can be decomposed as $\mu_j = |\mu_j|e^{\mathrm{i}\phi_j}$, with its modulus $|\mu_j|$ quantifying the growth (or decay) of the corresponding Floquet mode and ϕ_j representing its phase shift over a period. The stability of the periodic base solution is then addressed by considering the Floquet multiplier with largest modulus where if $|\mu_0|$ is greater than one the corresponding Floquet mode will grow over one period and the periodic base solution is unstable. When the leading Floquet multiplier is real ($\phi_0 = 0$), the Floquet mode is *synchronous* and the perturbation evolves in time with the period of the base flow. When the leading Floquet multiplier is complex ($\phi_0 \neq 0$) the mode is *asynchronous* and a frequency, denoted f' and related to the phase of the Floquet mode as $f' = \phi_0/(2\pi)$ is introduced.

To compute Floquet modes we employed the strategy proposed by Barkley & Henderson (1996). We assess the stability of an initial perturbation through the action of the propagator over one period $\mathbf{\Phi}$ – Monodromy matrix – whose action over the perturbation at an arbitrary

initial time t_0, formally denoted $\mathbf{q}'(\mathbf{x}, t_0 + T) = \mathbf{\Phi}\,\mathbf{q}'(\mathbf{x}, t_0)$, is obtained by time-integration along a period of the linearized equations (3.10). The boundary conditions (3.11), and the temporal and numerical discretization schemes previously described for the nonlinear method are again employed. An Arnoldi method with a modified Gram-Schmidt algorithm for the orthogonalization step (Saad 2011) is implemented in the FreeFEM software (Hecht 2012) to approximate the Monodromy matrix in a low-dimensional space. The eigenvalues of this reduced matrix approximate the Floquet multiplier and its eigenvectors allow reconstructing the Floquet modes at the initial time, i.e. $\hat{\mathbf{q}}(\mathbf{x}, t_0)$. A minimal number of 30 Arnoldi vectors is used in the following, this number being further increased in steps of 10 when necessary in order for the dominant eigenvalue to converge to five significant digits. All computed modes are normalised by the kinetic energy of the coupled fluid-solid system. This method has been equaly validated at (Benetti Ramos *et al.* 2020).

3.3. *Results of the SPW continuation with TSM and stability analysis*

Results of the continuation of the reversed Von Kármán wake (SPW) propulsive solutions with the TSM coupled to the pseudo arc-length and its fluid-solid Floquet stability are depicted in figure 4. TSM solutions were obtained for Stokes numbers $22.4 \leqslant \beta \leqslant 36$ by adopting an increasing and decreasing direction for the arc-length starting from the SPW propulsive solution for $\beta = 24$. Although a positive velocity is shown, a branch of negative velocity can equally be obtained. For increasing values of Stokes number ($\beta \geqslant 24$), the time-averaged velocity (4-a) increases monotonically along the branch, without passing through the velocity increase observed for DPW solutions for $\beta \geqslant 29$. The time-averaged vertical force (4-b) of the TSM solutions is always zero, differing from the DPW solutions found after $\beta \geqslant 27$. This fact is due to the conserved symmetry of the reversed Von-Kármán wake behind the foil, that will be further discussed in figure 5.

On the decreasing sense of Stokes number, a fold bifurcation is obtained at $\beta = 22.4$. In this saddle-node of periodic solutions, multiple solutions exist for a single value of Stokes number in the interval $22.4 \leqslant \beta \leqslant 23.5$. For $\beta = 23.5$ in the lower part of the saddle branch, the solution approaches a zero time-averaged velocity. A further continuation of the branch however did not reach symmetric non-propulsive solutions. Although possible, this continuation of the SPW branch has not been pursued as the results here described are sufficient to explain the transition to DQPW and DPW nonlinear regimes.

The fluid-solid Floquet stability analysis of the TSM branch identified two regions, dashed lines in figures 4 (a) and (b), where the leading Floquet multiplier (4-c) becomes unstable ($|\mu| > 1$). The first region occurs for $\beta \geqslant 27$, a region where TSM and unsteady nonlinear solutions present a disagreement concerning the time-averaged vertical force and the wake deviation, and unstable synchronous modes that do not modify the base-solution periodicity are obtained in this region. The saddle-node branch that appears for $22.4 \leqslant \beta \leqslant 23.5$, on the other hand, presents unstable asynchronous modes. In this second region, the branch becomes unstable shortly before ($\beta = 22.45$) the turning point of the fold bifurcation, and the unstable TSM solutions are mainly the coexisting limit cycles observed in figure 4 (a). We remark that, different than the case of fold bifurcation of steady solutions, the mode that becomes unstable is not necessarily a zero-frequency eigenvalue at the turning point Iooss & Joseph (1997). For $22.45 \leqslant \beta \leqslant 27$ the branch is thus stable, and we observed in (4-c) that the modes that become unstable in the saddle branch and for $\beta \geqslant 27$ belong to distinct branches. The asynchronous mode that is destabilized for $\beta = 22.45$ appears for $\beta \approx 23$ under the stable synchronous multiplier that is stabilized for $\beta \leqslant 27$. This branch of asynchronous multipliers ($|\mu| > 1$, $f' \neq 0$) and more precisely the multiplier destabilized for $\beta = 22.45$ introduce in the base solution a small frequency, whose evolution with the Stokes number is represented in figure (4-d), very similar to the one observed

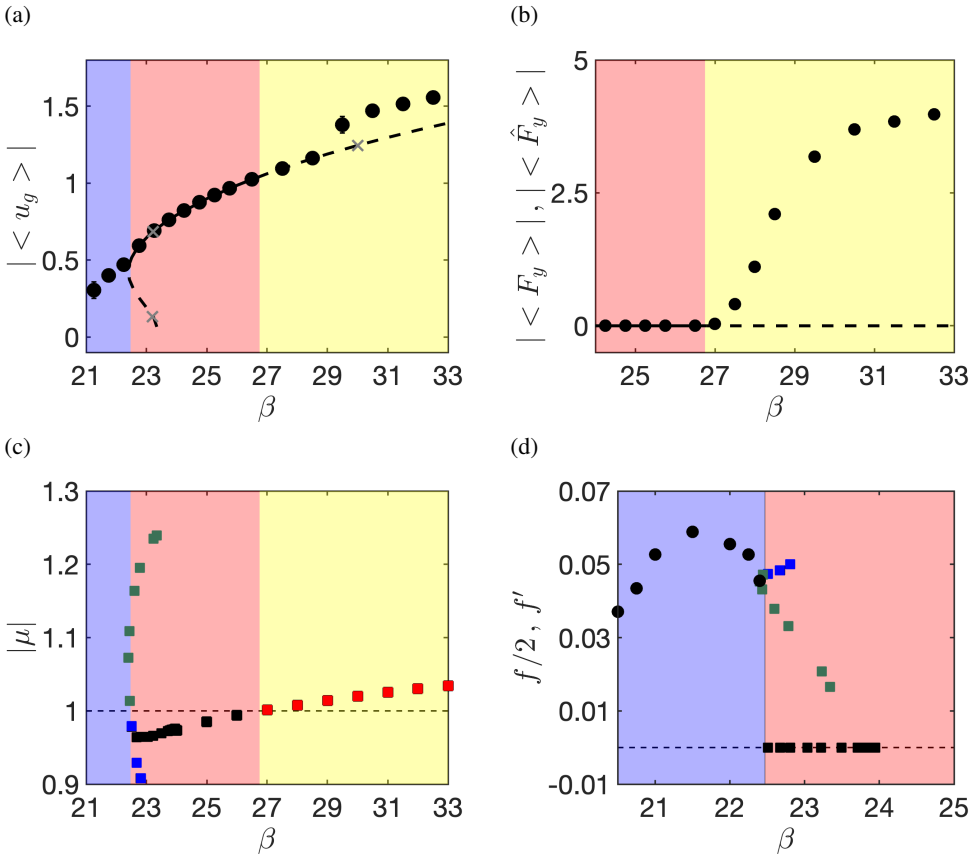

Figure 4: Time spectral method continuation (thick lines – solid/dashed lines indicating stable/unstable solutions) of SPW propulsive solutions and the branch fluid-solid Floquet stability (squares) compared to unsteady nonlinear results (circles). (a) Evolution of the absolute value of the time-averaged horizontal velocity and (b) vertical force as a function of the Stokes number β. The three grey $\times$ in (a) highlight solutions shown in Fig. 5. Leading Floquet multiplier (c) absolute value and (d) frequency evolution with the Stokes number – in (d) the frequency of the vertical force (half the one of the horizontal velocity $f/2$) is displayed for comparison. Stable (unstable) synchronous (asynchronous) modes are resp. identified by black (blue) and red (green) colors.

for the vertical force time signal (thus half the one of the velocity $f/2$) of DQPW propulsive solutions ($f' \approx 0.04 - 0.05$) that exist in the vicinity and in the threshold of the asynchronous multiplier.

To illustrate the evolution of the flow along this branch, the vorticity field of three solutions (highlighted in figure 4-a) is shown in figure 5 at several instant of the flapping period. All of these solutions are very similar to the SPW solutions previously shown in figure 1. Starting from $\beta = 30$, same value as the representative one used to illustrate DPW propulsive solutions in figure 1, we observe a SPW solution this time with a wake that does not deviate or break the spatio-temporal symmetry. As the Stokes number is decreased up to $\beta = 23.2$ the wake behind the flapping foil progressively decreases in length. Since the time-averaged horizontal velocity of the foil decreases, diffusive effects are intensified and become more visible in the wake behind the foil that is reduced until only a vortex dipole. The presence of this vortex dipole is a common feature of the solutions in the saddle branch even when the Stokes number increases (again for $\beta = 23.2$

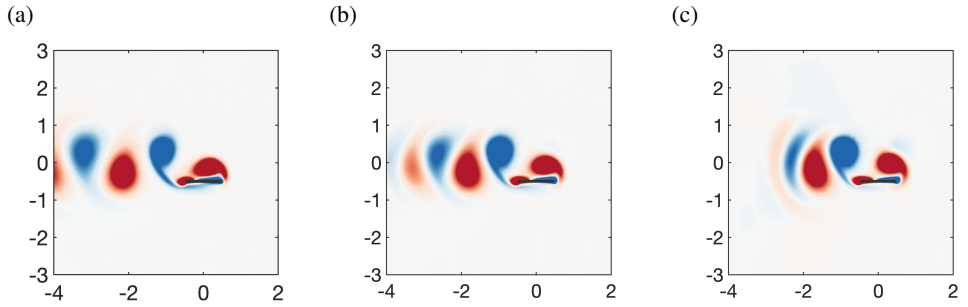

Figure 5: Symmetric periodic wake propulsive solutions obtained with the Time Spectral Methods. The three solutions represented are the grey × in figure 4 progressively decreasing the horizontal speed (a) $\beta = 30$, (b) $\beta = 23.2$ and (c) $\beta = 23.2$ (inside the saddle branch). The same scale as fig. 1 is used for the contours.

in c). The coexisting solutions for $22.4 \leqslant \beta \leqslant 23.5$ are thus one with a greater time-averaged horizontal velocity and a fully developed wake and another with a wake constituted of a vortex dipole with a smaller time-averaged velocity. All these solutions feature the same time-periodicity and behaviour of the horizontal velocity and vertical force of a typical SPW propulsive solution (as discussed in figure 2). The only remarkable difference between these solutions and the previously studied through unsteady simulations is the smaller horizontal speed for $\beta \geqslant 29$ and the zero average vertical force for $\beta \geqslant 27$.

To illustrate the collision of limit cycles that takes place at the saddle-node bifurcation we depict the phase portraits of horizontal force and velocity for different Stokes number in figure 6. For $\beta = 24$, before the range of coexisting solutions, only once limit cycle which has the shape of an ellipse is visible on the system. When the Stokes number is decreased up to $\beta = 22.6$ a second limit cycle of smaller horizontal velocity u_g and smaller horizontal force F_x amplitude appears in addition to the previous limit cycle, that suffers a decrease of its horizontal speed and force amplitude. As β is progressively decrease, these coexisting orbits approach themselves at $\beta = 22.45$, by this simultaneous increase/decrease of mean horizontal speed and force amplitude, up to the point of $\beta = 22.4$ when both orbits collide and only one limit cycle remains in the system. Add in the figure and illustrate the behaviour by restarting a simulation from the orange limit cycle down.

Since unstable modes are present either in the same region ($\beta \geqslant 27$) or in the vicinity (saddle-branch $\beta \approx 22.4$) of deviated periodic wake and deviated quasi-periodic wake propulsive solutions and feature a time-periodicity similar to these regimes, we study the characteristics of these modes in the following subsections to investigate if their internal mechanisms can shed further insights on the emergence of these nonlinear solutions.

3.3.1. *Synchronous wake deviation mode*

The unstable synchronous Floquet mode existent for Stokes numbers $\beta \geqslant 27$ is characterized for a representative value $\beta = 30$ in figure 7. As the action of this field is mainly observed over the wake behind the flapping foil, we depict the vorticity field through coloured filled contours at two equally spaced time instants along a flapping period in 7(a,b), where the contours of the base-flow, previously displayed in figure 5, are superposed using black (dashed) lines to represent positive (negative) vortex of its wake. This superposition reveals that the perturbation mainly consists of vortex dipoles acting on base-flow monopoles, and the mode bears a great similarity to the one obtained by Jallas *et al.* (2017) for the wake deviation of a non-propelled foil. Its instantaneous superposition over the base-flow (represented by thick black lines) is similar to

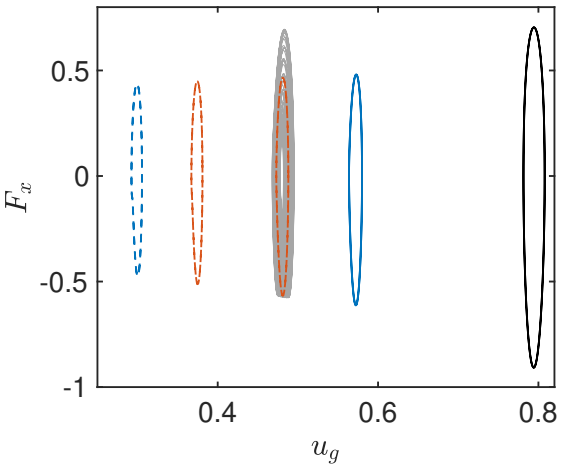

Figure 6: Phase portraits of horizontal force and velocity for three TSM solutions while decreasing the Stokes number: $\beta = 24$ (black lines) $\beta = 22.6$ (blue lines) and $\beta = 22.45$ (orange lines). For the two last values of Stokes number, there is two coexistent solutions. Solid lines represent stable solutions while dashed lines represent unstable solutions. The DQPW propulsive solution for $\beta = 22.4$ is added with a thin grey line. WITHDRAW THE BLACK ORBIT IN A AND ADD A FIGURE B WITH A ZOOM OF THE SUPERPOSITION OF TSM AND DNS NEAR THE DQPW – invert Fx in x axis and ug in y axis Transform in four figures: (a) zoom of the TSM - DNS comparison, (b) TSM, (c) DQPW, (d) going from the orbit with smaller velocity to the DQPW

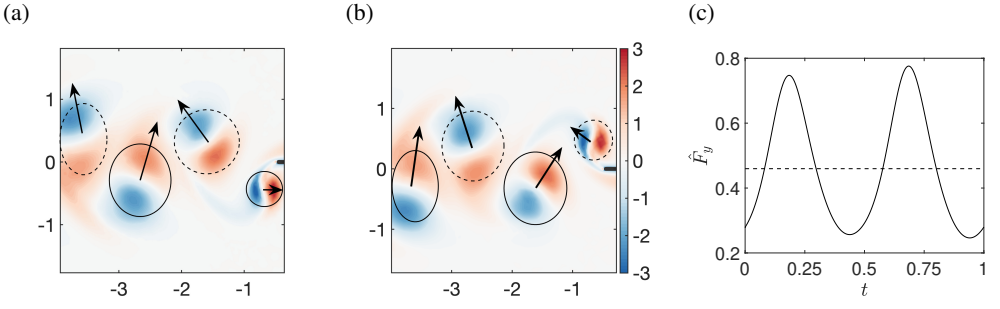

Figure 7: Unstable synchronous mode for $\beta = 30$: (a,b) vorticity contours for $t = 0.25$ and $t = 0.75$ and base flow positive (resp. negative) vortex contours represented by solid (resp. dashed) lines. Arrows indicate the core displacement of the base-flow vortex due to the perturbation. (c) Vertical force acting on the foil with its time-averaged value represented by a dashed line.

displacement modes Fabre *et al.* (2006); Brion *et al.* (2014) – the perturbation generates a net displacement of the vortex core due to simultaneous increase/decrease of the base-flow vorticity. As shown in figure 7(a,b), the effect of this perturbation over time instants (a) $t = 0.25$ and (b) $t = 0.75$ is to form vortex dipoles by approaching nearby vortices and displace the whole wake in the upward y direction, originating the wake deviation observed in nonlinear simulations. This upward deviation sustained across the whole period is a result of the mode spatio-temporal asymmetry – time instants separated by half a flapping period of the perturbation reflected at an inverse y position present the same vorticity as the previous half-stroke. As the mode is invariant in amplitude, a negative perturbation could equally sustain a downward wake deviation along

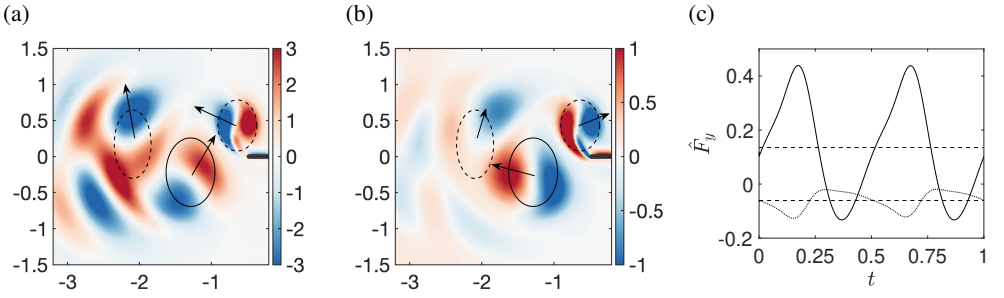

Figure 8: Unstable asynchronous mode for $\beta = 22.43$: vorticity contours of the (a) real part and (b) imaginary part for $t = 0.75$. Solid and dashed superposed thick lines represent positive and negative values of the base-flow vorticity. Arrows indicate the core displacement of the base-flow vortex due to the perturbation.(c) Real (solid line) and imaginary (dotted line) parts of the vertical force where a dashed line indicate its time-averaged value.

the flapping period. The vertical force acting on the foil, 7(c), is coherent to the wake deviation and oscillates around a non-zero time-average that is of the same sign of the wake deviation - an upward deviation (positive y) implies a positive time-averaged vertical force. Therefore, this mode is clearly at the origin of the emergence of the wake deviation and the non-zero time-averaged vertical force exhibited by deviated periodic wake (DPW) solutions in this Stokes number range.

This periodic wake deviation mode generates perturbations of the foil horizontal velocity and forces. Those are, however, not displayed since they present a very low amplitude, $O(10^{-3})$, undergoing positive and negative values along a flapping period thus oscillating around a zero time-average. This zero average allow us to understand why TSM and nonlinear simulations present the same average velocity for $27 \leqslant \beta \leqslant 29$, but it does not explain the increase of the average horizontal velocity observed for $\beta \geqslant 29$. Similar to the case of Jallas *et al.* (2017), this mode of wake deviation is incapable of explaining the increase the foil thrust, and in addition in our self-propelled setup, is incapable of producing a time-averaged increase of the foil horizontal velocity. We conceive again that nonlinear effects, observed to be the source of the sharp increase in the horizontal thrust Jallas *et al.* (2017) of non-propelled foils beyond the threshold of the Floquet instability, might play an important role on this horizontal velocity increase observed in our self-propelled simulations.

3.3.2. *Quasi-periodic wake deviation mode*

We now examine the asynchronous Floquet modes that gets unstable at the saddle-node branch. The mode obtained for $\beta = 22.4$ is displayed in figure 8. The instantaneous real and imaginary parts of the vorticity contours for $t = 0.25$ are displayed in 8(a,b). The amplitude of the real part is three times larger than the imaginary one but both their spatial structures consist of two very clear vortex dipoles centered around the first two base-flow monopoles (solid and dashed lines for positive and negative vorticity), as the synchronous modes. Further away, the perturbation slowly vanishes as diffusive effects come to play. Similar to the synchronous case, these two complex parts are again similar to vortex-core displacement modes. The orientation of the perturbation dipoles and thus their generated displacement is, however, quite different for each complex part, and an analysis of the mode reveals that while the real part tends to assemble the base-flow vortex in dipoles displaced upward, the imaginary part tend to separate the vortex. The real part effect is visibly of generating an approximation of the base-flow vortex into deviated dipoles, visible in 8(a). The perturbation superposed to the base-flow generates on the first (second) base-flow vortex starting at the trailing edge an increase of its negative (positive) vorticity on its upper

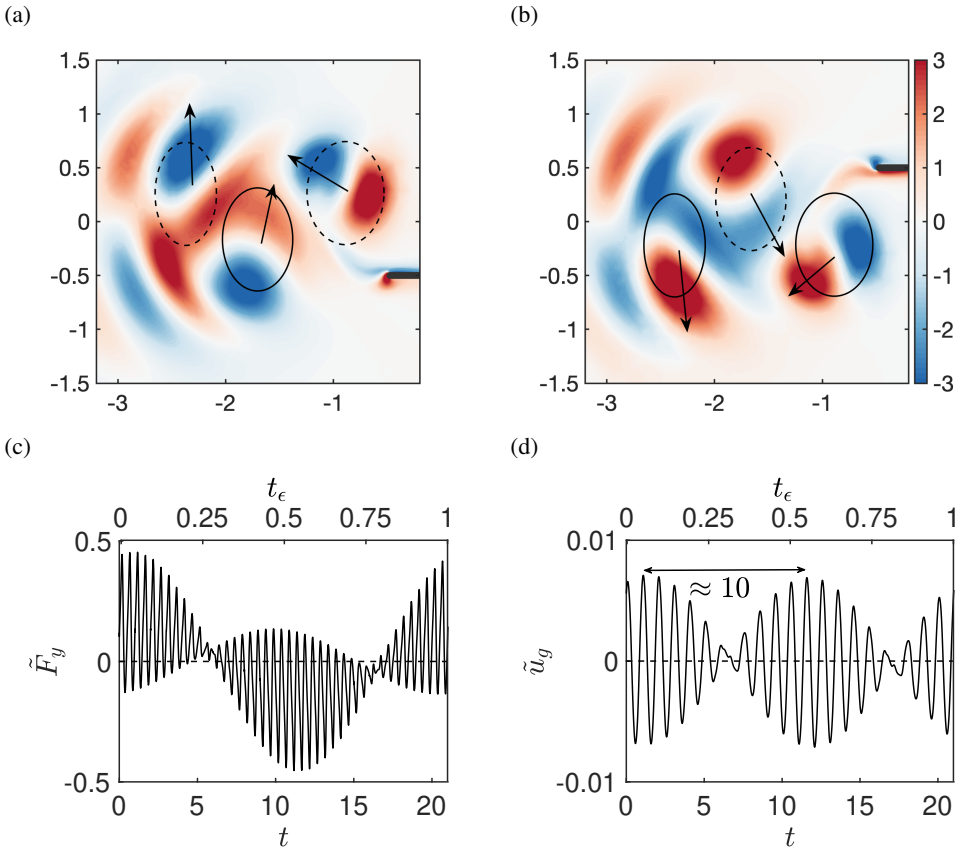

Figure 9: Temporal evolution of the quasi-periodic perturbation $\tilde{\mathbf{q}}$ for $\beta = 22.43$: (a,b) Vorticity of the perturbation (colors) and base-flow (with positive values in solid and negative in dashed lines) for $t_\epsilon = 0$ and $t_\epsilon = 0.5$ of the slow period $T_\epsilon = 1/f' = 23$. (c) Vertical force and (d) horizontal velocity. The time-averaged value of these quantities along the slow period is shown in (c,d) by a dashed line.

left (right) corner, resulting on the approximation of these vortex as to form a dipole displaced upward. The imaginary part, on the other hand, separate rather than assemble these two vortex near the trailing edge. In 8(b) for instance, the negative base-flow vortex is moved to the right by an increase of its vorticity on its right portion whereas the positive vortex is reinforced on its upper left portion.

These contrasting effects of the flow real and imaginary part are translated in their vertical force, figure 8(c). First of all, it is clearly seen by their superposition on the same figures that all real and imaginary quantities are out-of-phase. The real and imaginary part of the vertical force have opposite effects – the first one presents a positive time-average along a flapping period whereas the second one presents a negative one. The imaginary part has a much smaller amplitude than the real part owing to its smaller flow amplitude. The vertical force frequency is twice rather than one. This fact comes from the spatio-temporal asymmetry of the perturbation that results in an equal vertical force acting during upward and downward strokes. The horizontal velocity and force, as for the synchronous mode, oscillate around a zero time-averaged value, and have a small amplitude in both cases. The mode thus, do not generate in neither case an increase of the self-propelled velocity and it is not further discussed.

To further study the interplay of the mode real and imaginary parts we study the real *quasi-periodic* perturbation $\tilde{\mathbf{q}} = \mathbf{q}' e^{-\lambda_r t}$. Its temporal evolution can be developed as

$$\tilde{\mathbf{q}}(\mathbf{x}, t, t_\epsilon) = \Re(\hat{\mathbf{q}})(\mathbf{x}, t)\cos(2\pi t_\epsilon) - \Im(\hat{\mathbf{q}})(\mathbf{x}, t)\sin(2\pi t_\epsilon)\,, \tag{3.14}$$

where we have introduced the slow time scale $t_\epsilon = f' t$ since the frequency of the Floquet exponent $f' \ll 1$ is very small compared to the frequency of the Floquet mode. For $t_\epsilon \sim 0$, the quasi-periodic perturbation should be dominated by the real part of the periodic Floquet mode $\Re(\hat{\mathbf{q}})(\mathbf{x}, t)$, while for $t_\epsilon \sim 0.25$, it should be dominated by its imaginary part $\Im(\hat{\mathbf{q}})(\mathbf{x}, t)$. The quasi-periodic perturbation thus slowly evolves between the real and imaginary parts of the Floquet mode, on a time scale given by the low frequency of this asynchronous Floquet mode.

The temporal evolution of the quasi-periodic perturbation is displayed in figure 9. The quasi-periodic perturbation is similar to the real part of the Floquet mode at times $t_\epsilon = 0$ and $t_\epsilon = 0.5$, 9(a,b), where it respectively deviates the wake upward and downward, owing to change of sign due to the modulation of the Floquet multiplier imaginary part. The action of the real part of the Floquet mode are predominant when compared to the imaginary one, which is clear when analysing the forces acting on the foil and its horizontal velocity 9(c,d). For $t_\epsilon = 0.25$ and $t_\epsilon = 0.75$, all quantities are very small in amplitude and appear to be a simple transition between the switching of a positive and negative amplitude of the real part of the asynchronous mode. The switching between upward and downward deviation, for $t_\epsilon = 0$ and $t_\epsilon = 0.5$, is remarkably clear when regarding the vertical force 9(c) that assumes a positive and negative average values in these two time instants. The vertical force perturbation goes through positive and negative mean values following the wake upward and downward deviation, but oscillates along the slow period around a zero average. The horizontal velocity (d) present a different slow period than the vertical force. In both cases we observe a quasi-periodic oscillation around a zero average, as expected due to the zero-time average of both real and imaginary parts of the mode. Nevertheless, the slow period of these perturbations equals half the one of the vertical force and is thus ≈ 10 rather than ≈ 20. This fact is due to the similar effect in the horizontal dynamics of the foil generated by an upward or downward deviation of the wake as it was previously the case for DPW propulsive solutions.

The quasi-periodic perturbation generated by the unstable asynchronous mode generates a cycle of up and downward deviation of the wake along its slow period that results in an instantaneous increase of the vertical force but a zero time-average along the small period. The mode does not modify the base-flow time-averaged horizontal velocity and force, but introduces a slow period on the horizontal velocity that is equal to twice the one of the vertical force. These summed observations match completely the behaviour observed in the nonlinear simulations seen for DQPW propulsive solutions in figure 1. In addition, the fact that the perturbation does not alters the time-averaged horizontal velocity of the solution offers a possible explanation to the smooth transition between the mean horizontal speed of DQPW and SPW propulsive solutions obtained in unsteady nonlinear simulations (figure 3-a).

4. Global bifurcation from back & forth to deviated quasi-periodic wake propulsion

In the previous subsections Floquet stability analyses of the fluid-solid system were used to study the emergence of deviated quasi-periodic wake and deviated periodic wake propulsive solutions. This method was particularly adapted to these transitions, since they involved bifurcations of the SPW propulsive solution which is a periodic base solution. This is however not the case for the last transition between DQPW and back & forth propulsion, a transition that involves two quasi-periodic solutions. In this section outputs of unsteady nonlinear simulations will be used to

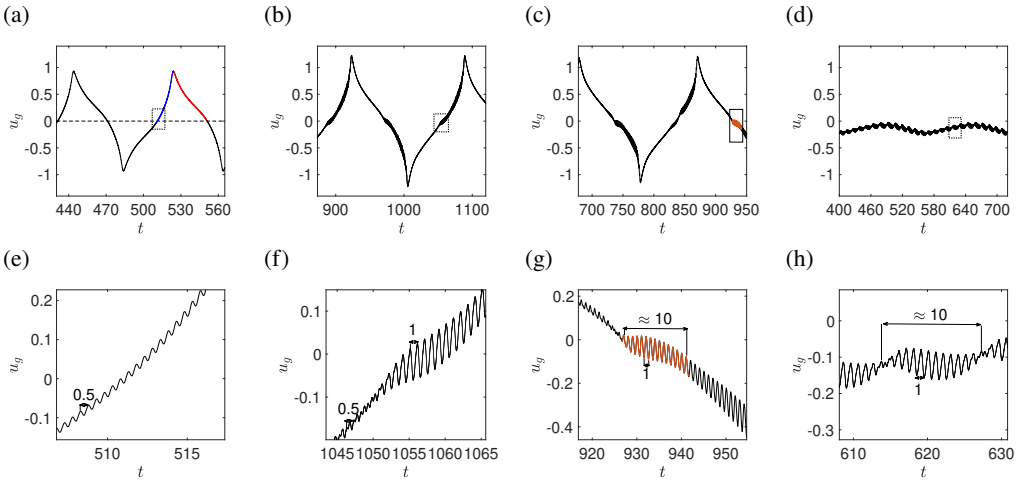

Figure 10: Transition from Back & Forth to deviated quasi-periodic wake Propulsive solutions: horizontal velocity time signals with close-up views for (a,e) $\beta = 17$, (b,f) $\beta = 19$, (c,g) $\beta = 19.5$ and (d,h) $\beta = 20.25$. Note that this last solution belongs to the DQPW propulsive solutions transition zone (hatched zone in figure 3) where two small frequencies are still found. In (a) the red and blue lines identify respectively time ranges where the velocity is accelerated and decelerated. In (c) the orange line identify a horizontal speed spot.

draw a better picture of this transition that is revealed to be a global bifurcation (Wiggins 1988) with DQPW propulsive and back & forth solutions colliding in the phase space.

To characterize this global bifurcation, we first investigate the appearance of horizontal velocity spots in back & forth solutions for $18 \leqslant \beta \leqslant 20$ where the amplitude of oscillation of this time signal suddenly increases, wake deviation appears and frequency modifications of the signal are observed. This analysis is followed by the study of the evolution with the Stokes number of phase portraits of horizontal velocity and force of the dynamical system where we highlight that, as β is increased, the back & forth solution starts to collide with the DQPW propulsive one.

Nonlinear simulations revealed that the transition between back & forth solutions and DQPW propulsion presents horizontal velocity spots for $18 \leqslant \beta \leqslant 20$. Figure 10 shows horizontal velocity time signals for (a-c) three back & forth and (d) the first obtained DQPW propulsive solution. These spots are evident when comparing the time signals of $\beta = 17$ and $\beta = 19$ in Fig. 10(a) and (b). In the first, the horizontal speed evolves in the time scale of one flapping period with a constant amplitude (the line presents a constant thickness) around the mean value that fluctuates between -1 and 1 due to the back & forth behaviour passing through acceleration and deceleration phases (that have been highlighted in blue and red for a positive velocity). In the second case, on the other hand, when the horizontal speed approaches 0, coming either from positive or negative values, its amplitude suddenly increases and we visualize a sudden thickening of the velocity amplitude. These thickening can be seen in the close-up views of figs. 10(e) and (f), where not only the increase of the amplitude of oscillation is comparable, but also we observe a switch of the horizontal velocity period from 0.5 to 1 when the spot is reached. Such period is typical of deviated wake propulsive solutions due to the loss of spatio-temporal symmetry, that is generated by the wake deviation for these two solutions.

The emergence of wake deviation is precisely observed in the flow for $\beta = 19$, represented in figure 11 for time instants equally separated in 15 flapping periods that are identified over a close-up of the horizontal velocity time signal in (11-a). As we see, starting at (11-c), the wake

behind the flapping foil for velocities close to 0 consist merely of a vortex dipole at the foil trailing edge. This dipole is deviated upward as the velocity changes of sign, becoming negative, and this deviated dipole (11-d,e) keep the normal suction effect at direction reversal of back & forth solutions as described in (Benetti Ramos *et al.* 2020). This deviated periodic wake thus justifies the unitary frequency observed in (10-f), and we remark that the observed deviation of the vortex dipole is very similar to the one observed for DQPW solutions, fig. 1. In (11-f), as the foil velocity increases,the vortex street looses its mean deviation and becomes an usual reversed Von-Kármán vortex street behing the foil trailing edge. The subsequent deceleration of the foil will shorten this wake up to a vortex dipole, that will again be deviated, this time downward rather than upward.

When the Stokes number β is further increased, the horizontal velocity spot will feature not only a wake deviation, but also an additional quasi-periodic behaviour. For $\beta \geqslant 19.5$, fig. 10(c), we highlight in orange along the time signal of the horizontal velocity the appearance a quasi-periodic spot of frequency $O(10^{-1})$. What differentiates this spot from the previous presented one at $\beta = 19$ are the facts that its time-averaged horizontal velocity becomes almost constants during a period ≈ 10 and that the amplitude of the horizontal velocity has an increase/decrease along this spot. The DQPW propulsive solutions that emerge close to the regime onset, such as the one depicted in figure 10 (d) for $\beta = 20.25$, exist exactly at the range $-0.2 < u_g < 0$ of the quasi periodic spot seen in (10-c). The spot observed for $\beta = 19.5$ is very similar to the $O(10^{-1})$ horizontal velocity oscillation of the DQPW propulsive solution, and this regime at its transition between back & forth and DQPW propulsion appear to be trapped within this spot since it still oscillates with a frequency of $O(10^{-2})$ characteristic of back & forth solutions. Furthermore, figure 11 reveals that the flow exhibited, depicted at the instants marked in 11(b), by this transitional solution is identical to the one presented by the spot at $\beta = 19.5$. At this time, however, no direction reversal and suction effect of the vortex is observed. A vortex pair is observed at the foil trailing edge, figure 11(g-j), the length of the vortex street periodically decreases (g-h) and increases (h-j) as the foil velocity oscillates with the very low frequency of back & forth solutions. The flow deviation is very similar to the back & forth spot (compare for instance 11 (d) and (j)) with a propulsive rather than suction effect of the vortex dipole being observed.

The summed observations of wake deviation, unitary frequency and the final quasi-periodic spots of horizontal velocity lead us to believe that the first DQPW propulsive solutions that appear in the transitional zone, hatched zone in figure 3(a), are oscillations with the low frequency of back & forth solutions that are trapped within a deviated quasi-periodic wake propulsive solution. The DQPW propulsive and back & forth solutions might thus be entangled in the phase space of dynamical systems and phase portraits might help us to better to characterize this collision. The phase portraits of horizontal speed and force (acceleration) associated to the previously discussed β are shown in figure 12. In this figures, the evolution of the horizontal velocity and force are depicted through the solutions slow period resulting in a closed curve drawn in the phase space.

The first three figures 12(a-c) represent the phase portraits of back & forth solutions. The structures depicted by these portraits are centered around the origin $(0, 0)$, which is consistent with the zero time-averaged velocity of these solutions and their self-propelled character (zero acceleration). The shape of a back & forth phase portrait is initially unperturbed for Stokes numbers up to $\beta = 17$, value that is depicted in figure 12(a). The obtained curve consists of similar structures for positive and negative velocity. Since the one in the side of the positive velocities adopt the same color code of figure 10(a), we can see that the portrait is composed for the positive velocities of an external/ red side structure (in blue) that corresponds to a time window where the positive velocity is being accelerated, and an internal/ left side structure (in red) instants where the velocity decays. When the velocity approaches zero it switches for the external structure of the negative velocities.

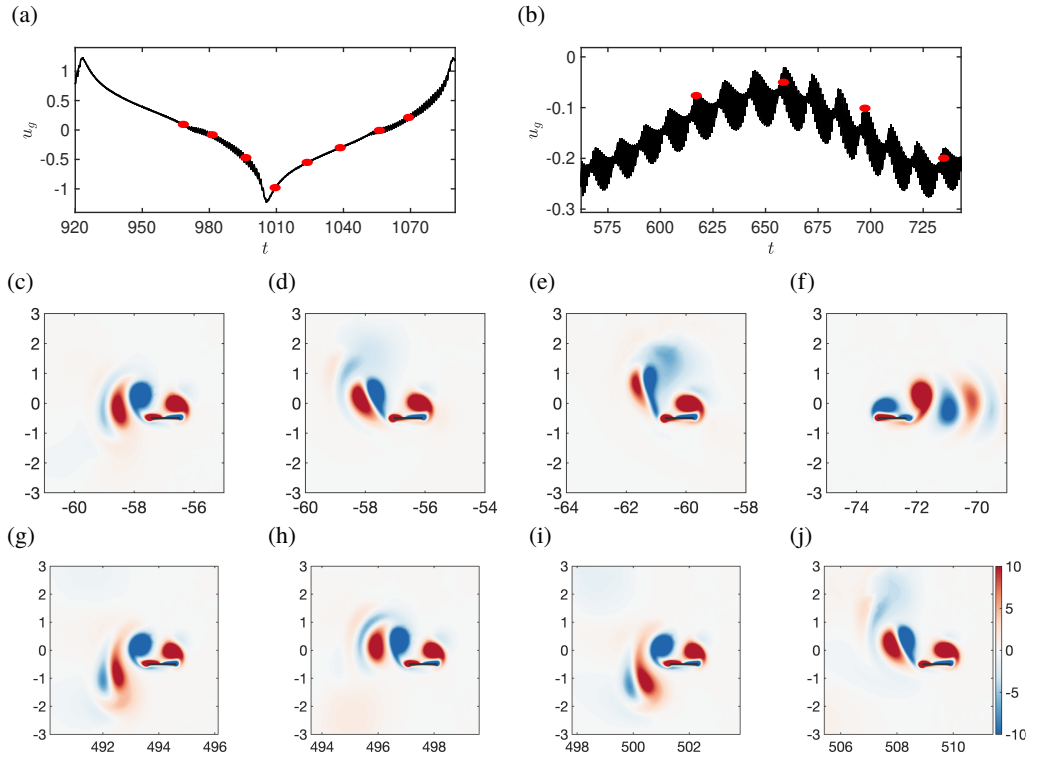

Figure 11: Back & Forth solution (β = 19 - (a) and (c-f)) and transition DQPW solution (β = 20.25 - (b) and (g-j)): (a,b) Horizontal speed time signals with red filled circles showing the equidistant time instants of (c-f) and (g-j) where the vorticity contours are presented. Images are presented in different horizontal positions.

The previously described phase portrait begins to be perturbed by the appearance of a secondary structure starting from β = 19. This structure is identified in (12-b) by a dotted orange rectangle, and it starts to grow precisely over the path followed by the decelerating structure previously depicted in red when the velocity changes of sign. This single structure becomes even more complex for β = 19.5 (12-c), being composed of two similar structures at opposite sides of the zero velocity where a bottle neck starts to appear. Again following the time signal of figure 10, the orange trace used to identify the quasi-periodic spot in this past figure help us to visualize that the secondary structure appearing on each side of the zero velocity is precisely the quasi-periodic spot previously identified in figure 10(c). The phase portrait of the DQPW solution for β = 20.25 is thus shown in figure 12 (d), and a remarkable similarity between the orange structure highlighted in (12 -c) and the phase portrait of the DQPW propulsive solution (in the transitional range where the low $O(10^{-2})$ remains) can be seen. The DQPW propulsive solution and the spot are centered around a negative time-averaged speed in this case and the slight displacement between the orange structure in (12 -c) and (12-d) might suggest that as the Stokes number is risen above the onset of DQPW propulsive solutions, the back & forth solution gets stuck at the DQPW propulsive orbit, suggesting a global bifurcation of the system. Since the frequency of back & forth solutions sharply decreases in Figure 3 (d) and the period of these solutions is heading towards infinity and a saddle-node of limit cycles is observed in our system, the scenario of a collision of a limit cycle with a saddle-node indicates that the dynamic system is passing through a *homoclinic bifurcation*

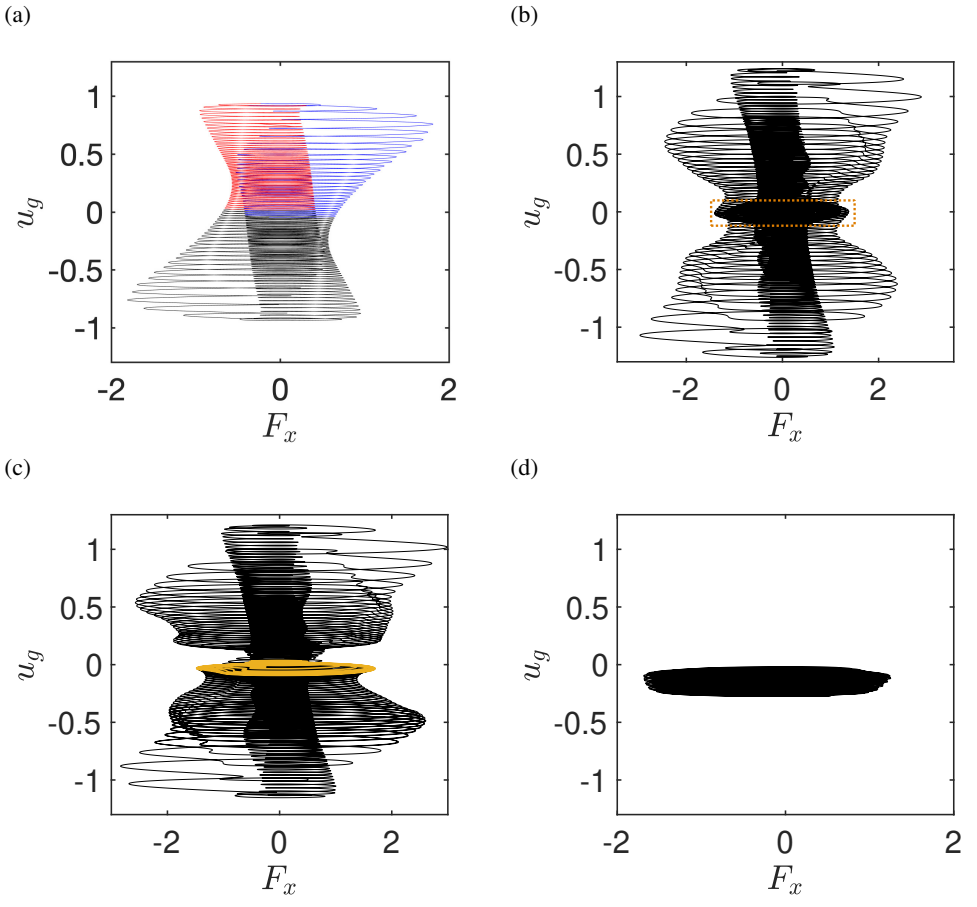

Figure 12: Transition from back & forth to deviated quasi-periodic wake propulsion: Phase portraits of the horizontal speed and force of (a-c) back & forth and (d) a deviated quasi-periodic wake propulsive solution for (a) $\beta = 17$, (b) $\beta = 19$, (c) $\beta = 19.5$ and (d) $\beta = 20.25$ previously presented in figure 10. In (a) and (c) we have adopted the same line color used in 10 for the horizontal speed acceleration and deceleration phases as well as the quasi-periodic spot.

Wiggins (1988); Schaeffer & Cain (2016) that results in the transition between back & forth and deviated quasi-periodic wake propulsive solutions.

5. Conclusions

In this work, we have studied the transition between self-propelled regimes of a heaving rectangular foil, immersed in a quiescent fluid, of aspect ratio $h = 0.05$, solid-fluid density ratio $\rho = 100$ and flapping amplitude $A = 0.5$ for Stokes numbers $10 \leqslant \beta \leqslant 40$. First, the occurrence of deviated quasi-periodic wake (DQPW), symmetric periodic wake (SPW) and deviated periodic wake (DPW) propulsive solutions was established using unsteady nonlinear simulations. Fluid solid Floquet stability analysis of symmetric non-propulsive solutions was thus performed for the investigated range of β. This study was followed by the nonlinear bifurcation of SPW propulsive solutions for $22.4 \leqslant \beta \leqslant 36$ and their fluid-solid Floquet stability analysis. This work was thus

concluded by an analysis of the summed up contributions of the nonlinear and linear analysis to understand the transition to the DQPW, SPW and DPW propulsive regimes.

First of all, we have shown using unsteady nonlinear simulations that the coupled fluid-solid system dynamics evolve while increasing β (as done for instance by Alben & Shelley (2005); Lu & Liao (2006)) from back & forth motion around a fixed point ($11.25 \leqslant \beta \leqslant 20$) to deviated quasi-periodic wake (DQPW) ($20.25 \leqslant \beta \leqslant 22.4$), symmetric periodic wake (SPW), $22.4 \leqslant \beta \leqslant 26.75$, finally reaching deviated periodic wake (DPW) propulsive solutions for $\beta \geqslant 27$. The results presented in this work highlight the existence of the intermediary state of deviated quasi-periodic wake propulsion between back & forth and SPW propulsive solutions, a regime to our knowledge not described in the literature.

The emergence of these nonlinear solutions was thus investigated by a fluid-solid stability analysis of symmetric non-propulsive solutions. This method, that was previously successful on the prediction of the onset of unidirectional and back & forth solutions for low Stokes numbers, did not allow to predict the onset of the three propulsive regimes obtained for higher Stokes numbers.

Nonlinear bifurcation methods were thus employed to follow SPW propulsive solutions. The time spectral method (TSM) coupled to pseudo arc-length continuation methods revealed that SPW solutions exist beyond their β range observed in unsteady nonlinear simulations. Particularly, the TSM revealed the existence of solutions that do not feature wake deviation in the range of DPW solutions, and that a saddle-node bifurcation of limit cycles exist on the vicinity of the transition between DQPW and SPW propulsive solutions.

Fluid-solid stability analyses of the TSM solutions were thus performed. Asynchronous unstable Floquet modes were obtained on the saddle-node branch, and synchronous unstable Floquet modes were found over the non-deviated periodic wake solutions for $\beta \geqslant 27$. In the case of the asynchronous unstable modes, vortex displacement modes responsible for the wake deviation are obtained. The quasi-periodic behaviour of the Floquet exponent translated by its slow period modulation generates a periodic upward and downward wake deviation. The quasi-periodic perturbation thus features instantaneous non-zero time-averaged vertical forces along flapping periods, but across the whole slow period the time-average of the vertical force is zero as so is the time-averaged horizontal force and velocity. The unstable synchronous Floquet modes are clearly similar to the wake deviation modes obtained by Jallas *et al.* (2017) for a non-propelled flapping foil and thus responsible for generating a wake deviation. The modes present thus a non-zero time-averaged vertical force and owing to their wake deviation that is a spatio-temporal asymmetry, result in a frequency of their horizontal force and speed equal to the flapping frequency. The time-average along a flapping period for the horizontal velocity and force are zero, and this mode does not affect then the self-propelled dynamics of the foil, only deviating the wake behind the foil.

The summed up contributions of unsteady nonlinear simulations, TSM and fluid-solid Floquet stability analyses have finally been used to study the transition between back & forth and deviated quasi-periodic wake propulsive solutions, DQPW and SPW solutions as well as SPW and DPW propulsive solutions. In the case of the transition between SPW and DPW propulsive solutions, the presence of the unstable synchronous modes responsible for the wake deviation of the symmetry preserved SPW solutions of the TSM branch is at the origin of the bifurcation observed in nonlinear simulations. Although this linear analysis correctly allowed us to predict the onset of DPW propulsive solutions and the emergence of a non-zero time-averaged vertical force and mean wake deviation, the linear analysis offer no possible insight for the increase of the time-averaged horizontal velocity obtained in nonlinear simulations. We have thus concluded that this increase might come from nonlinear effects. The transition between DQPW and SPW solutions is explained by the presence of unstable asynchronous Floquet modes of the saddle-node branch found by the TSM in the vicinity of the transition between these regimes. The quasi-periodic

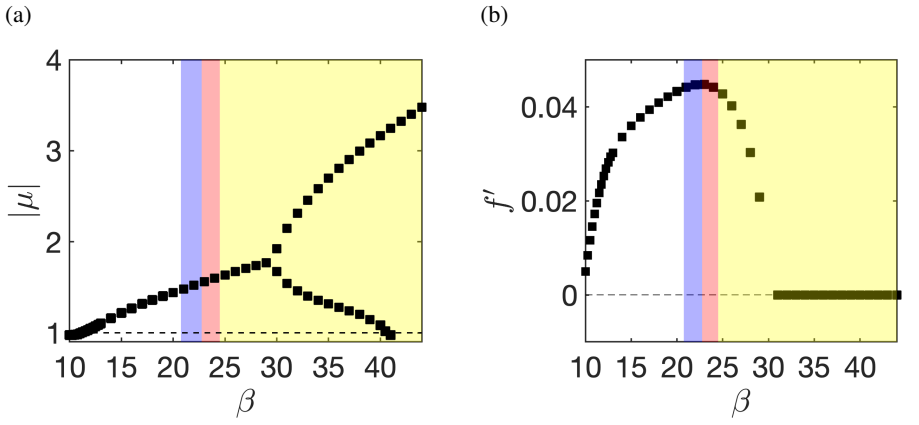

Figure 13: Fluid-solid stability analysis of non-propulsive solutions. (a) Absolute value and (b) frequency of the leading Floquet multiplier as a function of the Stokes number β. For comparison, the background colors violet, red and yellow indicate regions presenting quasi-periodic, reversed Von-Kármán wake and deviated wake propulsive solutions, as identified in §2.2

perturbation, as described above, features the periodic wake deviation and no increase of the time-averaged vertical force and horizontal velocity along a flapping period, being thus similar to DQPW propulsive solutions and explaining the smooth evolution of the horizontal velocity in this transition. The complex multiplier obtained by the fluid-solid Floquet stability analysis accurately predicts the low frequency of DQPW propulsive solutions in the critical threshold of the transition. We have finally explained the last transition between back and forth and deviated quasi-periodic wake propulsive solutions assembling elements of the unsteady nonlinear analysis and the TSM. The existence of the saddle-node bifurcation, the decrease of the frequency through the back & forth regime supported by the spots of horizontal speed present in back & forth solutions and the collision between revealed by the phase portrait drawn for this transition for $18 \leqslant \beta \leqslant 21$ lead us to conclude that this is a global bifurcation of homoclinic type.

We conclude through this study that the first transition to propulsion and the back & forth motion of a horizontally self-propelled flapping foil in a quiescent fluid are predictable by linear stability analysis. The further transitions that take place from back & forth motion to coherent propulsion, on the other hand, are nonlinear phenomena associated to a global and nonlinear bifurcations of the dynamical system. Appropriate nonlinear tools as time spectral methods associated to continuation methods should thus be employed to study these transitions.

Declaration of Interests: The authors report no conflict of interest.

Acknowledgments This project has received funding from the European Research Council (ERC) under the European Union Horizon 2020 research and innovation program (grant agreement No.638307)

Appendix A. Fluid-solid Floquet stability analysis of non-propulsive solutions

The emergence of the three regimes of QP, RVKW and DW propulsive solutions identified in the previous sections through nonlinear unsteady simulations is now investigated by analyzing the stability of non-propulsive periodic solutions. The symmetry preserved base-flow and the stability analysis applied in §2 are again employed. The coupled fluid-solid Floquet stability analysis around unstable non-propulsive solution for $\rho = 100$, $A = 0.5$ and $h = 0.05$ has been performed for

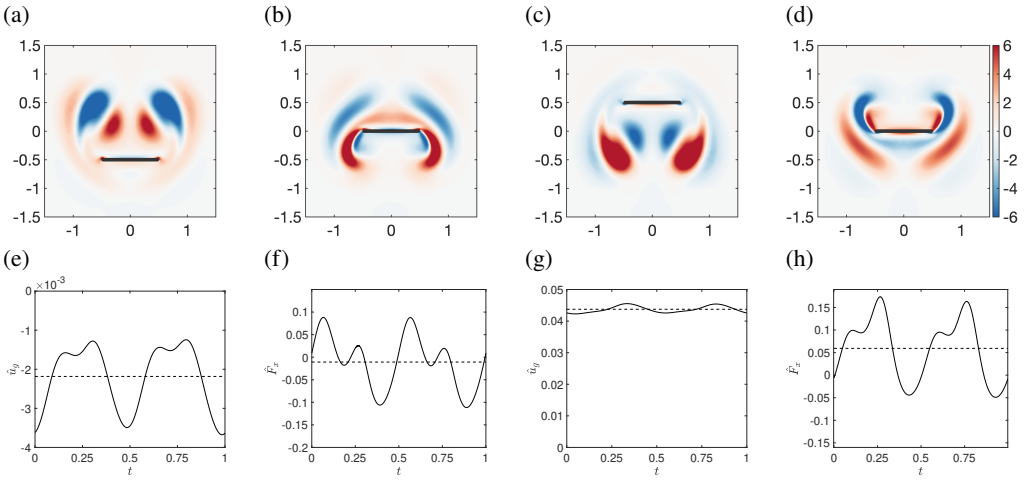

Figure 14: Leading and secondary unstable synchronous Floquet mode for $\beta = 35$: (a-d) Vorticity contours for four equally spaced time instants along a flapping period. Foil horizontal (e,g) velocity and (f,h) force respectively for the leading and secondary unstable multipliers. Mean force and speed in all figures represented by a dashed line.

$20 \leqslant \beta \leqslant 40$. We analyse in figure 13 the evolution with the Stokes number $10 \leqslant \beta \leqslant 40$ of the (a) modulus and (b) the frequency of the leading Floquet multiplier. We can clearly identify that for almost all the studied interval $\beta \geqslant 11.25$ the leading Floquet multiplier is unstable, being a pair of complex multipliers (asynchronous nature) for $11.25 \leqslant \beta \leqslant 30$. This pair of multipliers collapses on the real axis becoming two unstable synchronous modes for $30 \leqslant \beta \leqslant 41$ when one of the synchronous modes is stabilized. Since asynchronous (synchronous) Floquet multipliers (do not) break the time-periodicity of the base solution, the unstable modes share the time-periodicity of QP and DW propulsive solutions, for $\beta \geqslant 30$ in the former case, these modes will thus be analysed in the following paragraphs. The onset of the propulsive solutions, highlighted by the background colors in the figures, is not predicted by the destabilization of any mode.

Two unstable synchronous modes are obtained starting from $\beta = 30$. However, since both modes are very similar, we choose to represent only the least unstable one in figure 14 to analyse its characteristics. This mode is very similar to the real part of the asynchronous mode for $\beta = 21$, with an opposite sign. It breaks the left-right spatial symmetry and is again similar to a displacement mode. The mode is a propulsive one, but it does not break the spatio-temporal symmetry and no combination of this mode with a similar unstable one could result in the wake deviation observed in the nonlinear solutions at this Stokes number range.

The results of the Floquet stability around non-propulsive solutions do not match the unsteady nonlinear behaviour for $\beta \geqslant 20$. Although the quasi-periodic behaviour of the leading unstable mode is consistent with quasi-periodic propulsive solutions in the violet range of solutions, the dominant mode is similar to the one described in the previous chapter and presents a zero time-averaged horizontal velocity that matches further with back & forth solutions. When reversed Von-Kármán wake and deviated wake propulsive solutions are retrieved the leading unstable multiplier is still asynchronous in nature and there is no connection between the temporal dynamics predicted by stability and unsteady nonlinear analysis. The leading unstable synchronous mode or a combination of the unstable modes obtained for $\beta \geqslant 30$ cannot explain the wake deviation observed in this yellow region. We conclude thus that the transition between these different regimes – back & forth, QP, RVKW and DW propulsive regimes – cannot be explained by stability analyses of the non-propulsive symmetric base solution. To understand these transitions a different method

should be employed. In the following section, nonlinear methods will be introduced to sought for unstable base solutions near the observed transitions between QP, RVKW and DW propulsive solutions.

REFERENCES

Alben, Silas & Shelley, Michael 2005 Coherent locomotion as an attracting state for a free flapping body. *Proceedings of the National Academy of Sciences of the United States of America* **102** (32), 11163–11166.

Barkley, Dwight & Henderson, Ronald D. 1996 Three-dimensional Floquet stability analysis of the wake of a circular cylinder. *Journal of Fluid Mechanics* **322**, 215–241.

Barrett, David Scott 1996 *Propulsive Efficiency of a Flexible Hull Underwater Vehicle*.

Benetti Ramos, Luis, Marquet, Olivier, Bergmann, Michel & Iollo, Angelo 2020 Fluid-solid Floquet stability analysis of self-propelled heaving foils. *submitted to Journal of Fluid Mechanics* .

Brion, V., Sipp, D. & Jacquin, L. 2014 Linear dynamics of the lamb-chaplygin dipole in the two-dimensional limit. *Physics of Fluids* **26** (6).

Causin, P., Gerbeau, J. F. & Nobile, Fabio 2005 Added-mass effect in the design of partitioned algorithms for fluid-structure problems. *Computer Methods in Applied Mechanics and Engineering* **194** (42-44), 4506–4527.

Deng, Jian & Caulfield, C. P. 2015 Dependence on aspect ratio of symmetry breaking for oscillating foils: Implications for flapping flight. *Journal of Fluid Mechanics* **787**, 16–49.

Deng, Jian & Caulfield, C. P. 2018 Horizontal locomotion of a vertically flapping oblate spheroid. *Journal of Fluid Mechanics* **840**, 688–708.

Deng, Jian, Teng, Lubao, Caulfield, C. P. & Mao, Xuerui 2016 Instabilities of interacting vortex rings generated by an oscillating disk. *Physical Review E* **94** (3), 1–7.

Elston, John R., Sheridan, John & Blackburn, H. M. 2004 Two-dimensional floquet stability analysis of the flow produced by an oscillating circular cylinder in quiescent fluid. *European Journal of Mechanics, B/Fluids* **23**, 99–106.

Fabre, D., Citro, V., Sabino, D. Ferreira, Bonnefis, P., Sierra, J., Giannetti, F. & Pigou, M. 2018 A Practical Review on Linear and Nonlinear Global Approaches to Flow Instabilities. *Applied Mechanics Reviews* **70** (6).

Fabre, David, Sipp, Denis & Jacquin, Laurent 2006 Kelvin waves and the singular modes of the Lamb-Oseen vortex. *Journal of Fluid Mechanics* **551**, 235–274.

Faux, D., Thomas, O., Cattan, E. & Grondel, S. 2018 Two modes resonant combined motion for insect wings kinematics reproduction and lift generation. *Epl* **121** (6).

Floquet, G 1883 Sur les équations différentielles linéaires à coefficients périodiques. *Annales scientifiques de l'É.N.S. 2e série* **12**, 47–88.

Godoy-Diana, Ramiro, Marais, Catherine, Aider, Jean Luc & Wesfreid, José Eduardo 2009 A model for the symmetry breaking of the reverse Bénard-von Kármán vortex street produced by a flapping foil. *Journal of Fluid Mechanics* , arXiv: 0812.4137.

Gopinath, Arathi K & Jameson, Antony 2005 Time Spectral Method for Periodic Unsteady Computations over Two-and Three-Dimensional Bodies. In *43rd AIAA Aerospace Sciences Meeting and Exhibit*, pp. 1–14.

Govaerts, Willy J. F. 2000 *Numerical methods for bifurcations of dynamical equilibria*. Society for Industrial and Applied Mathematics.

Gray, J 1933 The movement of fish with special reference to the eel. *Journal of Experimental Biology* **10** (3), 88–104.

Hecht, Frédéric 2012 New development in freefem ++ Frédéric Hecht To cite this version : HAL Id : hal-01476313. *Journal of Numerical Mathematics* **20** (3), 1–14.

Iooss, Gerard & Joseph, Daniel D. 1997 Elementary Stability and Bifurcation Theory (Undergraduate Texts in Mathematics).

Jallas, Damien, Marquet, Olivier & Fabre, David 2017 Linear and nonlinear perturbation analysis of the symmetry breaking in time-periodic propulsive wakes. *Physical Review E* **95** (6), 1–15.

Jenny, Mathieu, Bouchet, Gilles & Dušek, Jan 2003 Nonvertical ascension or fall of a free sphere in a Newtonian fluid. *Physics of Fluids* **15** (1), L9–L12.

Jenny, Mathieu & Dušek, Jan 2004 Efficient numerical method for the direct numerical simulation of

the flow past a single light moving spherical body in transitional regimes. *Journal of Computational Physics* **194** (1), 215–232.

Kress, Wendy & Lötstedt, Per 2006 Time step restrictions using semi-explicit methods for the incompressible Navier-Stokes equations. *Computer Methods in Applied Mechanics and Engineering* **195** (33-36), 4433–4447.

Lu, Xi Y. & Liao, Qin 2006 Dynamic responses of a two-dimensional flapping foil motion. *Physics of Fluids* **18** (9).

Murphy, David W., Adhikari, Deepak, Webster, Donald R. & Yen, Jeannette 2016 Underwater flight by the planktonic sea butterfly. *Journal of Experimental Biology* **219** (4), 535–543.

Ramananarivo, Sophie, Godoy-Diana, Ramiro & Thiria, Benjamin 2013 Passive elastic mechanism to mimic fish-muscle action in anguilliform swimming. *Journal of the Royal Society Interface* **10** (88).

Ristroph, Leif & Childress, Stephen 2014 Stable hovering of a jellyfish-like flying machine. *Journal of the Royal Society Interface* **11** (92).

Saad, Yousef 2011 *Numerical Methods for Large Eigenvalue Problems*. Society for Industrial and Applied Mathematics.

Schaeffer, David G. & Cain, John W. 2016 *Ordinary Differential Equations: Basics and Beyond*, , vol. 65.

Schmid, Peter J., De Pando, Miguel Fosas & Peake, N. 2017 Stability analysis for n -periodic arrays of fluid systems. *Physical Review Fluids* **2** (11), 1–25.

Shaabani-Ardali, Léopold, Sipp, Denis & Lesshafft, Lutz 2017 Time-delayed feedback technique for suppressing instabilities in time-periodic flow. *PHYSICAL REVIEW FLUIDS* **2** (113904).

Shaabani-Ardali, Léopold, Sipp, Denis & Lesshafft, Lutz 2019 Vortex pairing in jets as a global Floquet instability: Modal and transient dynamics. *Journal of Fluid Mechanics* **862**, 951–989.

Sicot, F., Puigt, G. & Montagnac, M. 2008 Block-Jacobi Implicit Algorithms for the Time Spectral Method. *AIAA Journal* **46** (12), 3080–3089.

Sipp, Denis & Lebedev, Anton 2007 Global stability of base and mean flows: A general approach and its applications to cylinder and open cavity flows. *Journal of Fluid Mechanics* **593**, 333–358.

Tchoufag, Joël, Fabre, David & Magnaudet, Jacques 2014 Global linear stability analysis of the wake and path of buoyancy-driven disks and thin cylinders. *Journal of Fluid Mechanics* .

Triantafyllou, M. S., Triantafyllou, G. S. & Gopalkrishnan, R. 1991 Wake mechanics for thrust generation in oscillating foils. *Physics of Fluids A* **3** (12), 2835–2837.

Wiggins, Stephen 1988 *Global Bifurcations and Chaos - Analytical Methods*, , vol. 73, arXiv: arXiv:1011.1669v3.

Wu, Theodore Yaotsu 2010 A Review on Fish Swimming and Bird/Insect Flight. *Annual Review of Fluid Mechanics* **43** (1), 25–58, arXiv: 1006.1927.

Zhang, Xing, Ni, Saizhen, Wang, Shizhao & He, Guowei 2009 Effects of geometric shape on the hydrodynamics of a self-propelled flapping foil. *Physics of Fluids* **21** (10).